Electronic Structure Shift of Deeply Nanoscale Silicon by SiO$_2$ versus Si$_3$N$_4$ Embedding as an Alternative to Impurity Doping

Dirk König[1,*,†] Noël Wilck,[2] Daniel Hiller,[3] Birger Berghoff,[2] Alexander Meledin,[4,‡]
Giovanni Di Santo,[5] Luca Petaccia,[5] Joachim Mayer,[6,§] Sean Smith,[7,¶] and Joachim Knoch[2]

[1]*Integrated Materials Design Centre (IMDC) Node, University of New South Wales, NSW 2052, Australia*

[2]*Institute of Semiconductor Electronics (IHT), RWTH Aachen University, 52074 Aachen, Germany*

[3]*Research School of Engineering, The Australian National University, ACT 2601, Australia*

[4]*Ernst Ruska-Centre for Microscopy and Spectroscopy with Electrons (ER-C), Forschungszentrum Jülich GmbH, 52428 Jülich, Germany*

[5]*Elettra Sincrotrone Trieste, Strada Statale 14 km 163.5, 34149 Trieste, Italy*

[6]*Central Facility for Electron Microscopy, RWTH Aachen University, 52074 Aachen, Germany*

[7]*Department of Applied Mathematics, Research School of Physics and Engineering, The Australian National University, ACT 2601, Australia*

Conventional impurity doping of deeply nanoscale silicon (dns-Si) used in ultra-large-scale integration (ULSI) faces serious challenges below the 14-nm technology node. We report on a fundamental effect in theory and experiment, namely the electronic structure of dns-Si experiencing energy offsets of approximately 1 eV as a function of SiO$_2$ versus Si$_3$N$_4$ embedding with a few monolayers (MLs). An interface charge transfer (ICT) from dns-Si specific to the anion type of the dielectric is at the core of this effect and is arguably nested in the quantum-chemical properties of oxygen (O) and nitrogen (N) versus Si. We investigate the size up to which this energy offset defines the electronic structure of dns-Si by density-functional theory (DFT), considering the interface orientation, the embedding-layer thickness, and approximants featuring two Si nanocrystals (NCs), one embedded in SiO$_2$ and the other in Si$_3$N$_4$. Working with synchrotron ultraviolet- (UV) photoelectron spectroscopy (UPS), we use SiO$_2$- versus Si$_3$N$_4$-embedded Si nanowells (NWells) to obtain their energy of the top valence-band states. These results confirm our theoretical findings and gauge an analytic model for projecting maximum dns-Si sizes for NCs, nanowires (NWires), and NWells where the energy offset reaches full scale, yielding a clear preference for electrons or holes as majority carriers in dns-Si. Our findings can replace impurity doping for n- or p-type dns-Si as used in ultra-low-power electronics and ULSI, eliminating dopant-related issues such as inelastic carrier scattering, thermal ionization, clustering, out-diffusion, and defect generation. As far as majority-carrier preference is concerned, the elimination of those issues effectively shifts the lower size limit of Si-based ULSI devices to the crystallization limit of Si of approximately 1.5 nm and also enables them to work under cryogenic conditions.

I. INTRODUCTION

Impurity doping of Si has been a prerequisite for Si-based electronics for about 70 years [1]. Over the past

_____

*solidstatedirk@gmail.com

†Also at Institute of Semiconductor Electronics (IHT), RWTH Aachen University, 52074 Aachen, Germany

‡Also at Central Facility for Electron Microscopy, RWTH Aachen University, 52074 Aachen, Germany

§Also at Ernst Ruska-Center for Microscopy and Spectroscopy with Electrons (ER-C), Forschungszentrum Jülich GmbH, 52428 Jülich, Germany

¶Also at Integrated Materials Design Laboratory (IMDL), The Australian National University, ACT 2601, Australia

decade, impurity doping has gradually become a major issue in ultra-large-scale integration (ULSI) as fin and/or nanowire (NWire) device features have approached the characteristic lengths of dopant out-diffusion, clustering, and inactivation [2]. Considerable broadening of dopant profiles from drain and/or source regions into gate areas persists even when using self-regulatory plasma doping combined with rapid spike annealing [3]. Furthermore, the required ULSI transistor functionality [4] and emerging applications of Si nanocrystals (NCs) [5] have unveiled additional doping issues such as self-purification [6,7], dopant ionization failing at room temperature [8,9], and dopant-associated defect states [9–12]. As a result, the shrinkage of the physical field-effect transistor (FET) gate
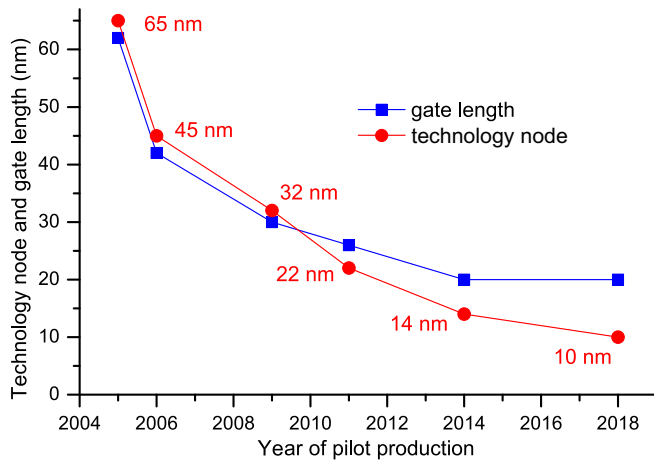
FIG. 1.   The evolution of Intel's ULSI technology nodes with the associated physical gate lengths of FETs [13]. The increasing gap between the node identifier and the actual gate length is evident.

length has increasingly lacked behind the characteristic length of the technology node and has remained constant at 20 nm since 2014, which has further increased the gap between the technology node and the actual gate length (see Fig. 1).

In the late 1970s, modulation doping of III-V semiconductor combinations such as GaAs/AlAs was discovered [14]. Lately, this concept has been applied successfully to Si by acceptor doping of adjacent SiO_2 [15–17] and has been proposed for donor-doping $Al_xGa_{1-x}N$ barriers from adjacent Si-rich Si_3N_4 during Si-NC formation annealing [18].

Ideally, a majority-carrier preference for electrons or holes and thus *n*- or *p*-type conductivity will not require doping if the electronic structure of the deeply nanoscale silicon (dns-Si) can be shifted over energy as per the *n*- or *p*-type section of an electronic device. Such an energy offset ΔE would avoid all of the dopant-related issues mentioned above, leading to lower inelastic-carrier scattering rates and higher carrier mobilities, which allow for decreased heat loss and bias voltages in ULSI. Together with directed self-assembly of block copolymers as a new approach to lithography [19], such properties enable Si-FET technology to work at yet smaller structure sizes, potentially enabling Moore's law to approach the Si crystallization limit of approximately 1.5 nm [20].

We have recently shown, in both theory and experiment, that ΔE exists in dns-Si when embedding one part of the Si nanovolume in SiO_2 and another part in Si_3N_4 [21]. However, a detailed investigation of the impact originating from interface bond densities per square, the thickness of the embedding dielectric, and the sample size on the magnitude of the effect has not been published yet. The latter is very important for the applicability of the effect in real devices. As an effect induced via the interface of dns-Si,

the extension of the *p*-*n* junction is on the order of approximately 15 Å, allowing for a leap in device miniaturization. Moreover, we deliver a detailed phenomenological description of the fundamental quantum-chemical origin of ΔE, which is underpinned by experimental data and DFT results.

In our work presented here, we consider SiO_2 and Si_3N_4 embedding of Si NCs as a function of the shape, size, interface orientation, and thickness of the embedding dielectric by using density-functional theory (DFT) to calculate their electronic structure. As the next step, we compute DFT approximants containing two NCs, one embedded in SiO_2 and the other in Si_3N_4, to verify the ΔE that we find for single Si NCs within one system, accounting for the interactions of both Si NCs. From there, we present experimental data on Si nanowells (NWells) embedded in SiO_2 versus Si_3N_4, namely information on the ionization energies of the valence-band edges of the Si NWells by long-term synchrotron ultraviolet-photoelectron spectroscopy (UPS) [21–26]. With this wealth of theoretical and experimental data, we propose a model explaining the interface impact of oxygen (O) and nitrogen (N) on dns-Si, the associated characteristic impact length, and other prominent features observed in the electronic structure of dns-Si. The massive ΔE observed in theory and experiment presents a fundamental effect that can replace doping by forcing dns-Si into *p*- or *n*-type carrier preference as a function of the embedding dielectric. Thereby, the advantages of fully depleted FET ULSI devices can be combined with carrier preferences hitherto only achieved by impurity doping on a miniaturization level, being far below current ULSI physical gate lengths.

II. METHODS

A. Density-functional theory calculations

Hybrid density-functional theory (h-DFT) calculations are carried out in real space with a molecular-orbital basis set (MOBS) and both Hartree-Fock (HF) and h-DFT methods as described below, employing the GAUSSIAN09 program suite [27]. Initially, the MOBS wave-function ensemble is tested and optimized for stability with respect to describing the energy minimum of the approximant (variational principle; stable = opt) with the HF method using a 3-21G MOBS [28] (HF/3-21G). This MO wave-function ensemble is then used for the structural optimization of the approximant, to arrive at its most stable configuration (maximum integral over all bond energies), again following the HF/3-21G route. Using these optimized geometries, their electronic structure is calculated again by testing and optimizing the MOBS wave-function ensemble with the B3LYP hybrid DF [29,30] and the 6-31G(d) MOBS [31] [B3LYP/6-31G(d)]. The root-mean-square (rms) and peak-force convergence limits are 8 and 12 meV/Å, respectively. Tight convergence criteria are applied to the self-consistent

field routine. Ultrafine integration grids are used throughout. During all calculations, no symmetry constraints are applied to MOs. The temperature of the approximants is set to $T = 300$ K for all calculations. Extensive accuracy evaluations can be found elsewhere [26,32,33]. We note that in real-space DFT calculations, exact calibration to an absolute energy scale (the vacuum-level E_{vac}) is known to be ambiguous [34]. Nevertheless, relative changes of energy values such as ΔE or fundamental energy gaps E_{gap} between approximants with different interface terminations are accurate within the same computation route, leaving a constant energy shift to all states with respect to E_{vac} as the only uncertainty. The approximants and MOs are visualized using GVIEW 5 [35]. The electronic density of states (DOS) is calculated from the MO eigenenergies, applying a Gaussian broadening of 0.2 eV. The sizes given for NCs, d_{NC}, are calculated as the product of the atomic volume of the Si and the number of Si atoms forming the NC, assuming a spherical shape. This approach allows for a direct comparison of results between approximants of different shape.

B. Sample preparation

Samples comprising a Si$_3$N$_4$-embedded NWell are fabricated by plasma-enhanced chemical-vapor deposition (PECVD), using SiH$_4$ + NH$_3$ + N$_2$ for the Si$_3$N$_4$ buffer and the top layers (thickness 5.5 and 1.5 nm, respectively) and SiH$_4$ + Ar for amorphous Si [36]. The thickness of the Si$_3$N$_4$ spacer layer serves to suppress excited electrons from the Si wafer from interfering with electrons from the Si NWell during UPS. The substrates, i.e., n-type Si wafers (Sb doping, 5–15 × 10^{-3} Ω cm) of (111) surface orientation, are wet-chemically cleaned. After deposition, the wafers are annealed in a quartz tube furnace for 1 min at 1100 °C in pure N$_2$ ambient to induce Si crystallization. Subsequently, samples are H$_2$ passivated at 450 °C for 1 h.

Samples comprising a SiO$_2$-embedded NWell are dry etched with an isotropic SF$_6$/O$_2$ plasma to thin down an 85-nm-thick top c-Si layer of a Si-on-insulator (SOI) wafer with 200 nm of buried SiO$_2$ (BOX), to arrive at approximately 2.7–6.5-nm-thick c-Si on top. The back etch is followed by oxidation in 68-wt% HNO$_3$ at 120 °C, resulting in a 1.1–5.0-nm Si NWell with a 1.4-nm SiO$_2$ capping.

Si reference samples are processed by etching an (001) Si wafer (Sb-doped n type, 5–15 × 10^{-3} Ω cm) in 1-wt% buffered hydrofluoric acid and immediate sample mounting under a N$_2$ shower, with swift loading into the ultrahigh-vacuum (UHV) annealing chamber.

All NWell samples are contacted via a lateral metal contact frame on the front surface, which is processed by photolithographical structuring, wet-chemical etching in 50% HF plus 0.1% HNO$_3$ for opening the top Si$_3$N$_4$ or in 1-wt% hydrofluoric acid for opening the top SiO$_2$
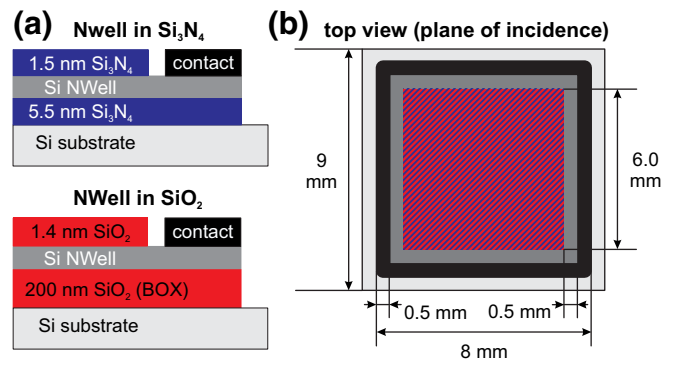

FIG. 2. (a) A cross-section view of the sample layout of Si NWells embedded in Si$_3$N$_4$ or SiO$_2$ for synchrotron UPS measurements, showing the edge region of the samples. (b) The top view of the plane of incidence, with the mesastructure inside the contact frame: the hatched area denotes the respective dielectric.

layer, and thermal evaporation of 300 nm Al, followed by a lift-off in dimethyl-sulfoxide [H$_3$C—(S═O)—CH$_3$]. The Si reference samples are contacted directly on their front surface. Figure 2 shows the structure of the mesa samples.

C. Characterization

Ultraviolet-photoelectron-spectroscopy (UPS) measurements are carried out at the BaDElPh beam line [37] at the Elettra Synchrotron in Trieste, Italy (see Ref. [21] for details). All samples are subject to a UHV anneal for 90 min at 500 K to desorb water and air-related species from the sample surface prior to the measurements. Single scans of spectra are recorded over 12 h per NWell sample and subsequently added up to eliminate white noise. Scans for the Si reference sample are recorded over 2 h and subsequently added up [21]. All samples of beam time 1 are exited with photon energies of $h\nu = 8.7$ eV and a photon flux of 2 × 10^{12} s^{-1}. Samples of beam time 2 are excited with $h\nu = 8.0$ eV and a photon flux of 2 × 10^{12} s^{-1}, yielding a slightly better signal-to-noise ratio (SNR) due to an increased inelastic mean free path λ_{IMFP} of the escaping electrons. The incident angle of the UV beam onto the sample is 50° with respect to the sample-surface normal and excited electrons are collected using an electron analyzer along the normal vector of the sample surface. The energy calibration of the UPS is realized using a Ta stripe in electrical contact with the sample as a work-function reference. Further UPS data for the SiO$_2$ and Si$_3$N$_4$ reference samples as well as on the UPS signal normalization and background substraction are available in Refs. [21,26] and in the Appendix.

All samples for transmission-electron-microscopy (TEM) investigation are capped with a protective 100-nm-thick SiO$_2$ layer to facilitate the preparation of cross sections by the focused-ion-beam (FIB) technique using a

FEI Strata FIB 205 work station. Some samples are further thinned by means of a Fischione NanoMill. TEM analysis of the cross sections is performed using a FEI Tecnai F20 TEM operated at 200 kV at the Central Facility for Electron Microscopy, RWTH Aachen University, and using the spherical-aberration-corrected FEI Titan 80-300 TEM operated at 300 kV at the Ernst Ruska-Centre, Forschungszentrum Jülich [38].

In addition, the Si NWell thicknesses are measured by ellipsometry. The thicknesses of the Si NWells in Si_3N_4 and in SiO_2 are measured using a Woollam M-2000 ellipsometer and an ACCURION nanofilm ep4se ellipsometer, respectively. All of the thickness measurements are confirmed by values obtained from TEM. However, the samples are given a standard deviation in NWell thickness of ± 1 monolayer (ML) due to the large extension of the measurement spot during UPS as compared to the NWell thickness.

III. DFT RESULTS

Our previous DFT calculations evaluated the electronic structure of Si NCs by substituting N for O atoms at the Si NC-SiO_2 interface [33], as a function of the NC size and of the thickness of the embedding dielectrics SiO_2 and Si_3N_4 [21]. Here, we evaluate the impact of the interface orientation and extend the size range to yet larger Si NCs, into their experimentally relevant size range, with varying thickness of embedding dielectric through long-term DFT computations. Additionally, we combine two Si NCs—one embedded in SiO_2 and the other in Si_3N_4—into one approximant for Si_{35} (11-Å), Si_{84} (15-Å), and Si_{165} (19-Å) NCs as the ultimate test of the entire electronic material system within one DFT approximant.

A. Single Si NCs coated with SiO_2 versus Si_3N_4

With the interface charge transfer (ICT) at the core of ΔE, we investigate the nature of the interface and the interface-to-volume ratio of dns-Si as key parameters defined by the system size. The latter can be expressed by the ratio of interface bonds to the number of Si NC atoms N_{IF}/N_{NC} [39], whereby this ratio can be applied to other dns-Si volumes such as NWires or fins [40]. Apart from its termination with OH versus NH_2 groups, the nature of the interface is defined by its orientation with characteristic bond densities per square. We choose the $\langle 111 \rangle$ and $\langle 001 \rangle$ orientations with their interface bond densities per cm^2 of $\square N_{111} = 7.8 \times 10^{14}$ cm^{-2} and $\square N_{001} = 13.6 \times 10^{14}$ cm^{-2} [41], respectively, for two reasons. First, the technologically most relevant interface orientations of dns-Si are $\langle 001 \rangle$, $\langle 110 \rangle$, and $\langle 111 \rangle$. Second, $\square N_{110} = 9.6 \times 10^{14}$ cm^{-2} for the $\langle 110 \rangle$ orientations of the Si interfaces [41] is close to $\square N_{111}$, a significant difference of its impact on the ICT is not given. We calculate octahedral approximants with exclusive $\langle 111 \rangle$ orientations
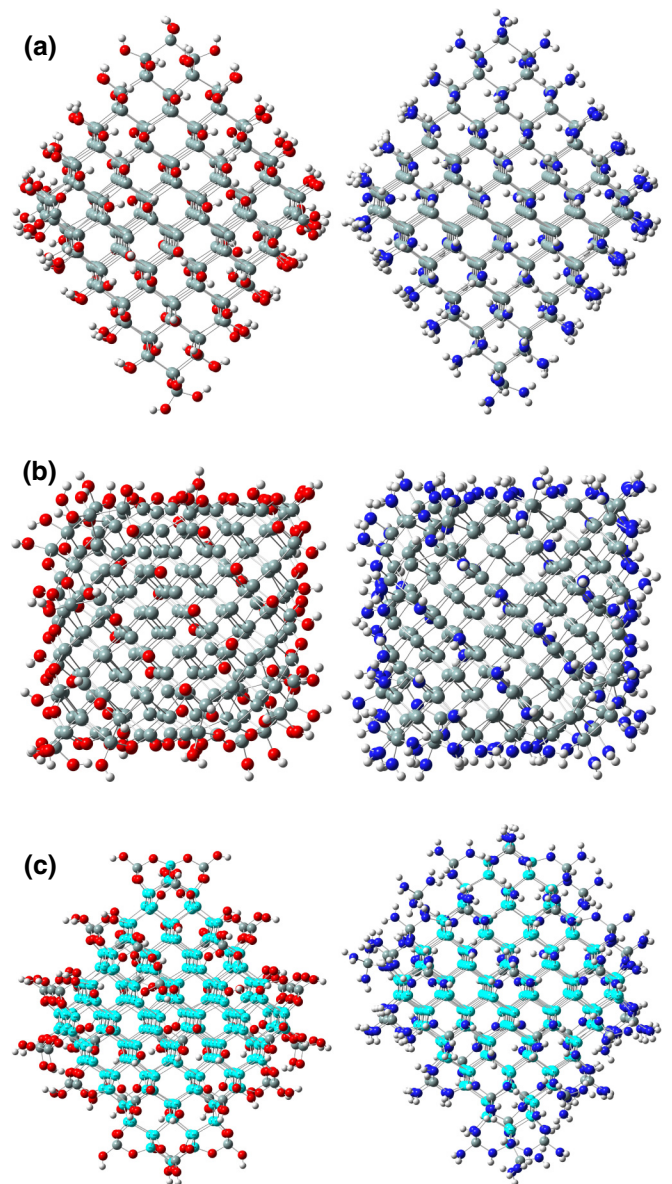

FIG. 3. Approximants to explore the impact of interface modification on the electronic structure of Si NCs. (a) Octahedral $\langle 111 \rangle$-faceted Si NCs ($Si_{286}X_{144}$, $X =$ OH, NH_2) of size 22 Å. (b) Cubic $\langle 001 \rangle$-faceted Si NCs [$Si_{216}(>XH_{-1})_{75}X_{48}$, $>XH_{-1} =>$ O/NH] of size 20.2 Å. (c) The same Si NCs as shown in (a), embedded in 1.5-ML SiO_2 or Si_3N_4: the NC atoms are highlighted in cyan. Atom colors: Si is gray, O is red, N is blue, and H is white.

up to $d_{NC} = 25.9$ Å—$Si_{455}X_{196}$ with $X =$ OH, NH_2 [see Fig. 3(a)]—and cubic approximants with exclusive $\langle 001 \rangle$ orientations and associated bridge bonds (>) of NH and O groups up to $d_{NC} = 20.2$ Å—$Si_{216}(>XH_{-1})_{75}X_{48}$ with $XH_{-1} =>$ O/>NH [see Fig. 3(b)]. Computations of larger cubic NCs such as $Si_{512}(>XH_{-1})_{75}X_{48}$ are not successful due to the excessive strain induced by >NH and, in particular, >O causing the cubic shape to disintegrate.
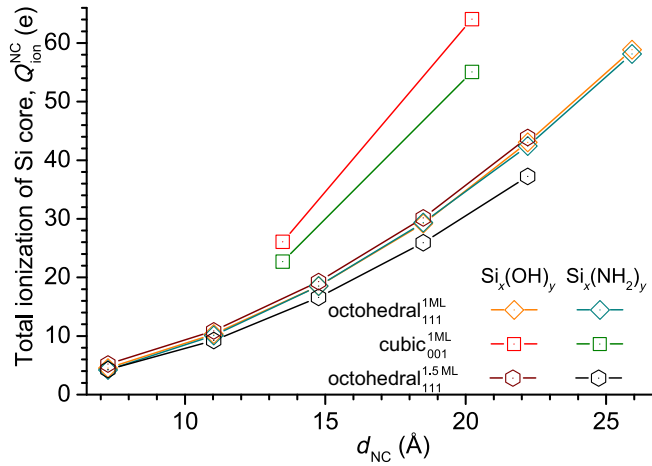
FIG. 4. The total ionization of the Si NCs of the NC classes shown in Fig. 2. Terminations with OH (NH$_2$) are considered to present 1 ML of SiO$_2$ (Si$_3$N$_4$).

Another important parameter is the thickness of the embedding dielectric. We calculate octahedral Si NCs with exclusive $\langle 111 \rangle$ orientations as above, but covered in 1.5-ML SiO$_2$ or Si$_3$N$_4$ up to Si$_{286}$ NCs ($d_{\mathrm{NC}} = 22.2$ Å). Thereby, we can directly compare the electronic structures of both approximant cohorts. Figure 3(c) shows such approximants, where the NCs have been highlighted.

We now focus on the ionization of Si NCs (see Fig. 4). This provides a blueprint for the strength of the ICT, which is closely linked to ΔE. All total NC ionizations $Q_{\mathrm{ion}}^{\mathrm{NC}}$ over d_{NC} show a quadratic dependence, which clearly points to a surface effect [33,39]. In general, O-terminated species have a slightly higher ionization, although the difference in ionicity of the Si—O bond, with approximately 53% ionic, versus the Si—N bond, with approximately 35%, is significant [32,42]. The minute difference for OH- and/or NH$_2$-terminated octahedral NCs shows that the ICT is saturated for $d_{\mathrm{NC}} \leq 25.9$ Å. As we will see in Sec. V, this value is merely limited by the tractable DFT system size and is surpassed roughly threefold when feeding experimental results into an analytic impact model of ΔE [33]. Accordingly, the embedding of Si NCs into 1.5-ML SiO$_2$ only yields a slightly higher value of $Q_{\mathrm{ion}}^{\mathrm{NC}}$, whereby the ionization drops notably when coating in 1.5-ML Si$_3$N$_4$. The origin of the latter is due to the positive electron affinity X of N, which deflects the valence-electron wave functions originating from Si NC atoms, resulting in a delocalization of these wave functions (see Sec. V for details). As a consequence of delocalization, part of the Si-NC charge is reflected back into the NC, thereby lowering its positive ionization. Due to MO hybridization, the unoccupied states follow suit and show a similar localization behavior. Considering $Q_{\mathrm{ion}}^{\mathrm{NC}}$ as a function of the interface orientation, it becomes apparent that $\langle 001 \rangle$-faceted interfaces with their increased bond density yield a stronger

ICT. A direct comparison of $N_{\mathrm{IF}}/N_{\mathrm{NC}}$ between $\langle 001 \rangle$-cubic versus $\langle 111 \rangle$-octahedral NCs cannot be accomplished due to their different d_{NC} values. As a good estimate, we can compare the average value of the Si$_{165}X_{100}$ and Si$_{286}X_{144}$ NCs of $N_{\mathrm{IF}}/N_{\mathrm{NC}} = 0.555$, with their average size of $d_{\mathrm{NC}} = 20.4$ Å, to $N_{\mathrm{IF}}/N_{\mathrm{NC}} = 0.917$ for the $\langle 001 \rangle$-cubic approximant Si$_{216}(>XH_{-1})_{75}X_{48}$, with $d_{\mathrm{NC}} = 20.2$ Å [39]. We obtain 5/3 of the number of interface bonds per NC atom when going from $\langle 111 \rangle$-octahedral to $\langle 001 \rangle$-cubic NCs. Accordingly, $\langle 001 \rangle$-cubic NCs are significantly more ionized than $\langle 111 \rangle$-octahedral NCs (see Fig. 4).

Alternations of the ICT as a function of the interface orientation and the thickness of the embedding dielectric lead to a modification of the NC electronic structure, namely the energies of the highest occupied MO (HOMO) E_{HOMO} and of the lowest unoccupied MO (LUMO) E_{LUMO} (see Fig. 5). The increased ICT due to a higher $N_{\mathrm{IF}}/N_{\mathrm{NC}}$ ratio for $\langle 001 \rangle$-cubic NCs or due to increasing the dielectric embedding from 1 to 1.5 MLs results in a more pronounced shift with respect to the vacuum level E_{vac}. For N-terminated NCs, a more pronounced shift toward E_{vac} is clearly visible for the $\langle 111 \rangle$-octahedral NCs embedded in 1.5-ML Si$_3$N$_4$ and, in particular, for the $\langle 001 \rangle$-cubic NCs. The results for O-terminated $\langle 111 \rangle$-octahedral NCs show the same trend, with more pronounced shifts further below E_{vac}. The cubic NCs Si$_{64}(>O)_{27}(OH)_{30}$ ($d_{\mathrm{NC}} = 13.5$ Å) and Si$_{216}(>O)_{75}(OH)_{48}$ do not follow the trend, which appears surprising at a first glance. When looking at the latter cubic Si NC [see Fig. 3(b)], we see that considerable strain deforms the NC cube. For $\langle 111 \rangle$-octahedral NCs, strain has only a minor influence on their electronic structure even with embedding (see Fig. 3 and Ref. [21]). However, with many >O bond configurations on the $\langle 001 \rangle$ interfaces, strain may become more influential on the electronic structure, as is evident from comparing the bond lengths and angles (cf. Table I). The O—Si bonds in
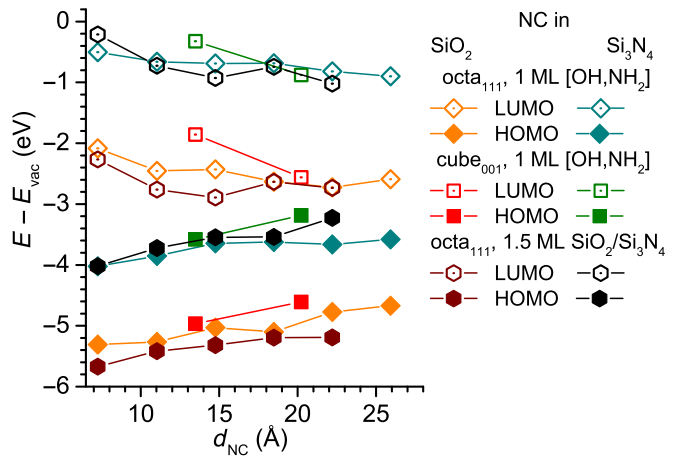

FIG. 5. The HOMO and LUMO energies relative to E_{vac} of the NC classes shown in Fig. 3. Terminations with OH (NH$_2$) are considered to present 1 ML of SiO$_2$ (Si$_3$N$_4$).

TABLE I.   The bond lengths $d_{\text{Si}—X}$ ($X = $ O, N) of the bridging anion species >O or >NH, the bond angles over the associated Si atoms $\angle_{X—\text{Si}—X}$, and the bond angles $\angle_{\text{Si}—\text{Si}—\text{Si}}$ over Si—Si—Si in the center of cubic NCs, shown for 20.2-Å cubic Si NCs with exclusively $\langle 001 \rangle$-oriented interfaces [cf. Fig. 3(b)]. For comparison, the $d_{\text{Si}—X}$ bond lengths of SiO₂ and Si₃N₄ approximants are listed. All lengths and angles are given as average values with absolute standard deviations. All approximants have identical parameters in HF/3-21G structural optimization.

	$\text{Si}_{216}(>\text{O})_{75}(\text{OH})_{48}$	SiO₂ [$\text{Si}_{29}\text{O}_{76}\text{H}_{36}$]
$d_{\text{Si}—\text{O}}$ (Å)[a]	1.732 ± 0.031	1.612 ± 0.009 [26]
$\angle_{\text{O}—\text{Si}—\text{O}}$ (deg)	132.86 ± 1.24	
$\angle_{\text{Si}—\text{Si}—\text{Si}}$ (deg)[b]	109.76 ± 0.91	
	$\text{Si}_{216}(>\text{NH})_{75}(\text{NH}_2)_{48}$	Si₃N₄ [$\text{Si}_{40}\text{N}_{86}\text{H}_{98}$]
$d_{\text{Si}—\text{N}}$ (Å)[c]	1.824 ± 0.032	1.757 ± 0.016 [26]
$\angle_{\text{N}—\text{Si}—\text{N}}$ (deg)	125.19 ± 1.27	
$\angle_{\text{Si}—\text{Si}—\text{Si}}$ (deg)[b]	109.75 ± 0.96	

[a]Excluding –OH groups.
[b]Angle from central Si atom up to 2ⁿᵈ nearest neighbor Si.
[c]Excluding –NH₂ groups.

ultrathin SiO₂ at the NC are approximately 7.4% longer when compared to SiO₂, while the value for the Si—N bonds is stretched by a mere 3.8% with respect to Si₃N₄ [26]. A similar situation exists with the Si—Si—Si bond angles when going from the NC center to its interface. Together with a bond energy of $E_{\text{bond}}(\text{Si}—\text{O}) \approx 4.72$ eV versus $E_{\text{bond}}(\text{Si}—\text{N}) \approx 3.89$ eV [42], the combination of a higher E_{bond} and shorter bond lengths shows that >O bond configurations to Si are capable of generating notably more local strain as opposed to >NH bond configurations. With O-terminated $\langle 001 \rangle$-cubic NCs, it appears that significant strain lowers the binding energy of the system, which is reflected in a slight shift toward E_{vac} (see Fig. 3). It has been reported that strain dominates the electronic structure of even $\langle 111 \rangle$-octahedral Si NCs embedded in SiO₂ [43], although we cannot confirm such results with our own calculations of such Si NCs in up to 3 MLs of SiO₂ [21]. Hence, only massive strain emerges as a modifier of the electronic structure, although it is still exceeded considerably by the impact of the embedding dielectric via ICT.

In summary, we observe a substantial energy offset of the electronic structure of Si NCs terminated with O versus N, yielding $\Delta E_{\text{HOMO}} \approx 1.75$ eV and $\Delta E_{\text{LUMO}} \approx 1.93$ eV with a 1.5-ML coating of SiO₂ versus Si₃N₄. These values correspond to approximately 75% and 55%, respectively, of the nominal HOMO-LUMO gap of Si NCs in the size range of 20 Å. We find that the ICT is dominated by bond densities per square given by the interface orientation via

the ratio $N_{\text{IF}}/N_{\text{NC}}$ and to a lesser degree by the thickness of the embedding dielectric. Interface strain originating from >O bonds has a minor influence on the electronic structure by decreasing the binding energies of $\langle 001 \rangle$-cubic NCs. This decrease in binding energy shifts their electronic structure slightly toward E_{vac}, opposing the downshift of the electronic structure by SiO₂ embedding to some extent.

B. One approximant featuring a Si NC in SiO₂ adjacent to a Si NC in Si₃N₄

An approximant consisting of two Si NCs, with the first (second) NC embedded in SiO₂ (Si₃N₄), presents the ultimate DFT system with which to test the energy offset ΔE and to gain further insight into its working principle. We calculate four approximants that mainly differ in the size of the embedded Si NCs: $2 \times \text{Si}_{10}$ (7.2 Å each) [21], $2 \times \text{Si}_{35}$ (11.0 Å each), $2 \times \text{Si}_{84}$ (14.8 Å each), and $2 \times \text{Si}_{165}$ (18.5 Å each). The latter two NC sizes overlap with experimental observations, thus providing a solid ground for Sec. V where we estimate the size range up to which dns-Si systems are dominated by ΔE.

Figure 6 shows the results for the $2 \times \text{Si}_{35}$, $2 \times \text{Si}_{84}$, and $2 \times \text{Si}_{165}$ approximants, with the respective DOS ranges enlarged to show the localization of the electronic states within the approximants. Beneath these DOS ranges, isodensity plots of the partial DOS located predominantly within one of the NCs are shown as a function of their embedding. We can clearly see two effects: ΔE_{HOMO} and ΔE_{LUMO} increase, with the NC separation growing with the NC size [44]. The global energy gap of the entire approximant $E_{\text{gap}}^{\text{global}}$ decreases with NC size. Both effects lead to a superlinear increase in the n- or p-type preference for charge carriers with an increasing NC size (cf. Fig. 7) and, in general, with the size of the dns-Si systems up to a certain limit (see Sec. V). We note that the ΔE_{HOMO} and ΔE_{LUMO} values of the $2 \times \text{Si}_n$ approximants ($n = 10, 35, 84, 165$) do not reach the values obtained for individual NCs in Sec. A. The proximity of SiO₂ to Si₃N₄ results in a transient region in which the electron-localizing nature of O cancels out with the electron-delocalizing nature of N [21]. Since the combined thickness of SiO₂ and Si₃N₄ between the NCs gets thicker with an increasing NC size, this effect diminishes, to yield increased values of ΔE_{HOMO} and ΔE_{LUMO}.

The total NC ionization in Fig. 7 shows only minor deviations from the ionization of $\langle 111 \rangle$-octahedral NCs with an OH or NH₂ termination (see Fig. 4), confirming that both 18.5-Å Si NCs (Si₁₆₅) are still within the range of ICT saturation. These minor deviations are instructive in understanding the impact of O versus N on dns-Si (see Sec. V).

For all NC sizes, N-terminated Si NCs increase their ionization slightly from coverage with all-around 1.5-ML Si₃N₄ via inclusion into 1–3-ML Si₃N₄ in $2 \times \text{Si}_n$
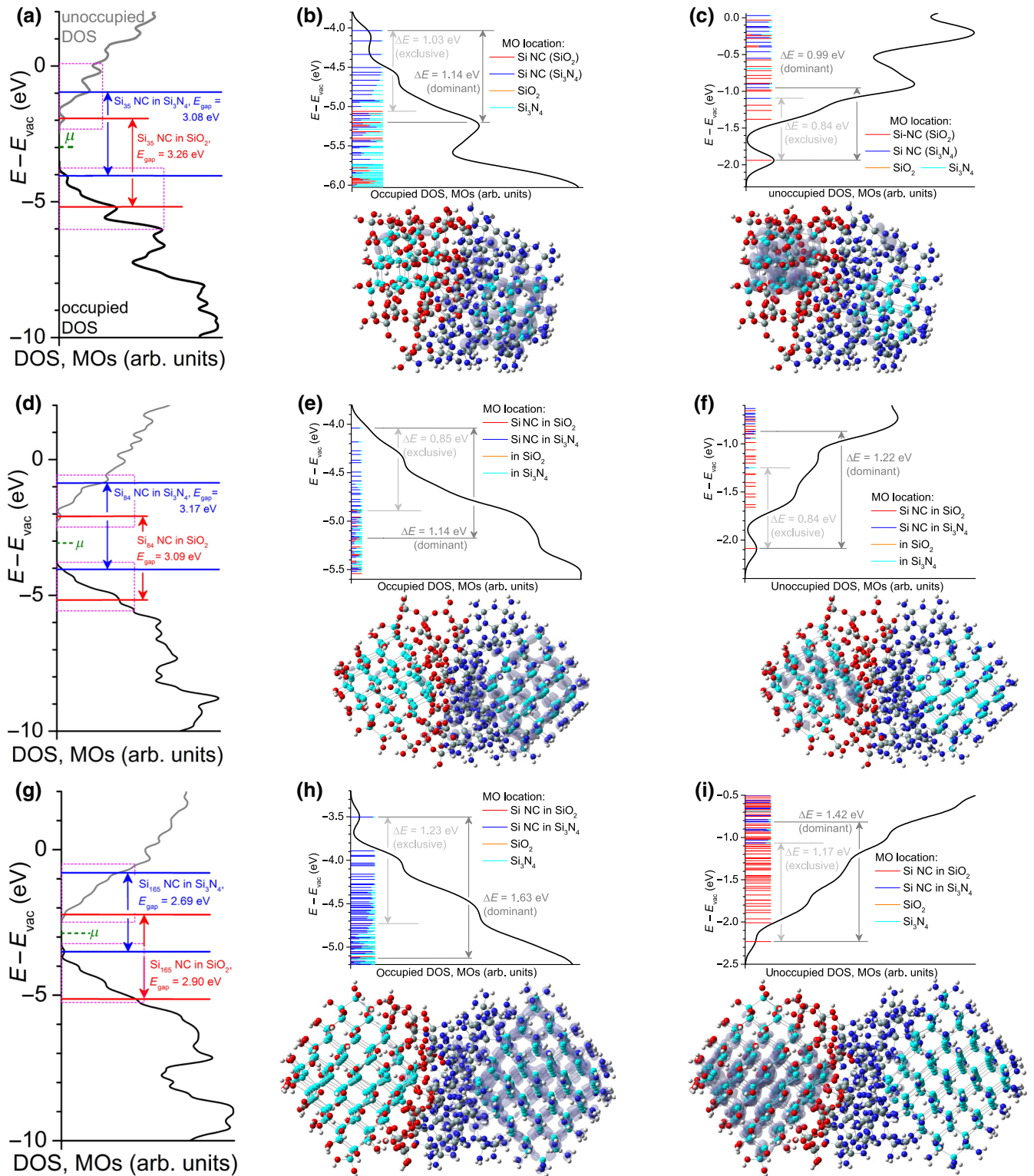
FIG. 6.   The DFT results of two embedded Si NCs in SiO₂/Si₃N₄ within one approximant. (a) The DOS of the $2 \times$ Si$_{35}$ NCs, of size 11.0 Å: the green dashed line shows the chemical potential μ of the approximant. (b) The detailed DOS of frontier OMOs contained in the magenta rectangle, showing their localization, together with an isodensity plot of the OMOs (4.6×10^{-3} $e/a_{B,0}$) within the energy window in which the NC in Si₃N₄ dominates the electronic structure. (c) The detailed DOS of frontier UMOs contained in the magenta rectangle, showing their localization, together with an isodensity plot of the UMOs [3.2×10^{-3} $e/a_{B,0}$] within the energy window in which the NC in SiO₂ dominates the electronic structure. All of the isodensity plots have the same value per frontier OMOs or UMOs. Graphs (d)–(f) show results for $2 \times$ Si$_{84}$ NCs of size 14.8 Å and graphs (g)–(i) for $2 \times$ Si$_{165}$ NCs of size 18.5 Å. For the atom colors, see Fig. 3.
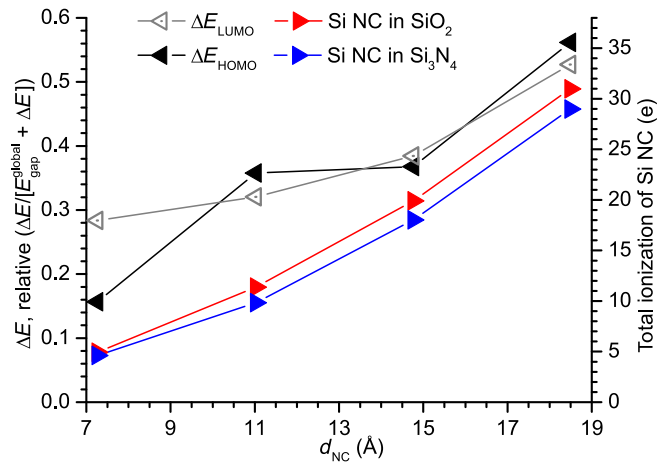
FIG. 7. The relative change in the OMO and UMO energy offsets due to SiO_2 versus Si_3N_4 embedding as function of the NC size, referring to the global HOMO-LUMO gap of Si NCs in SiO_2 versus Si_3N_4 (see Fig. 6). The colored symbols show the total Si-NC ionization as a function of the NC size and embedding and refer to the right-hand scale.

approximants up to all-around 1-ML Si_3N_4 coverage. As pointed out in Sec. A, this increase with a decreasing thickness of the Si_3N_4 embedding originates from the positive electron affinity X of N. The 1–3-ML Si_3N_4 coverage takes an intermediate position between the full-coverage values with 1- and 1.5-ML Si_3N_4. In other words, the 1-ML Si_3N_4 coverage of the outer NC interface in $2 \times Si_n$ approximants does not delocate and/or deflect valence-electron wave functions originating from Si NC atoms sufficiently to provide a full upshift of energy levels. Arguably, and backed by experimental data (Sec. IV), the electronic states of the Si_3N_4-embedded NCs in the $2 \times Si_n$ approximants can be located nearer to E_{vac} if a complete multi-ML embedding in Si_3N_4 with >1500 heavy atoms can be computed.

For Si NCs in SiO_2, the NC ionization increases from 1-ML via 1.5-ML SiO_2 to embedding in 1–3-ML SiO_2 in $2 \times Si_n$ approximants. Here, the strong localization of the valence electrons from the Si NCs at O drives the ionization process and thus the shift of the valence-electron wave functions of the Si NC to higher binding energies. We can thus presume an average 2-ML embedding in SiO_2 for the $2 \times Si_n$ approximants, yielding 1, 1.5, and 2 MLs for the increasing ionization of the Si NCs by SiO_2, which clearly correlates with the number of O atoms per Si-NC atom.

To recapitulate, ΔE also exists in the complete system manifested by $2 \times Si_n$ approximants, one embedded in each of SiO_2 and Si_3N_4. The strength of ΔE increases with the NC separation given by the combined inter-NC thickness of SiO_2 and Si_3N_4, although it does not quite reach the values for individual NCs in SiO_2 versus Si_3N_4. As a likely cause, we identify the transition range between SiO_2 and Si_3N_4, where the natures of the two anions—O and N—tend to cancel each other's impact on the electronic

structure. Apart from proving the full scale of ΔE in a complete system, the $2 \times Si_n$ approximants investigated in this section yield more detailed evaluations of NC ionization and ΔE.

IV. EXPERIMENTAL RESULTS: SYNCHROTRON UPS

After initial UPS measurements confirming the effect of ΔE for Si NWells in SiO_2 versus Si_3N_4 [21], we characterize ten SiO_2- and four Si_3N_4-embedded NWells with thicknesses ranging from 11 to 50 Å. Since we work with NWells and thus quasi-2D band structures, we replace E_{HOMO} and E_{LUMO} with the energies of the highest occupied—namely, top valence-band—states E_V and of the lowest unoccupied—namely, bottom conduction-band—states E_C, respectively, to account for the limits on continuous electronic DOS. Details on deriving the ionization energy $E_{ion} = E_V$ of such valence-band states and the respective standard deviations can be found in the Appendix and in Ref. [26]. Figure 8 shows the E_V values as a function of the NWell thickness d_{NWell} for SiO_2 and Si_3N_4 embedding.

For $d_{NWell} = 11$–15 Å, we obtain $E_V \approx E_{vac} - 5.85$ eV for NWells in SiO_2 and $E_V \approx E_{vac} - 4.96$ eV for NWells in Si_3N_4. For SiO_2 embedding, a minute change to $E_V \approx E_{vac} - 5.82$ eV occurs for $d_{NWell} = 25 \pm 1$ Å. The changes are more notable for Si_3N_4 embedding, where we obtain $E_V \approx E_{vac} - 5.08$ eV for $d_{NWell} = 27$ Å. We also note that $E_V(d_{NWell})$ changes rather continuously as compared to NWells embedded in SiO_2, which is the subject of discussion in Sec. V. In the range of $d_{NWell} \approx 30$–40 Å, the E_V values of the Si NWells in SiO_2 and Si_3N_4 change to approach the common value $E_V = E_{vac} - 5.17$ eV, as is
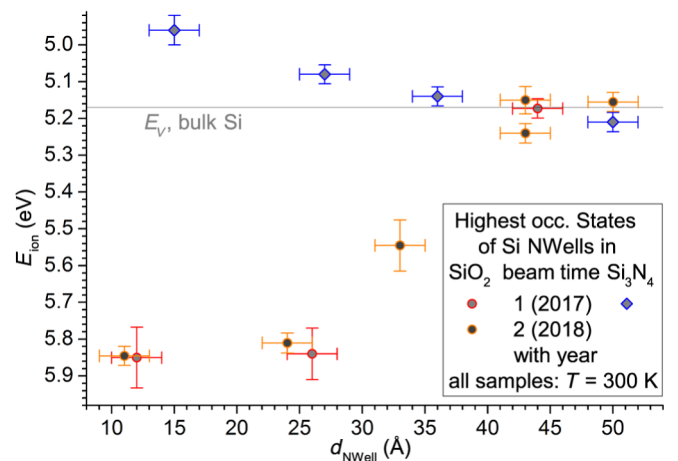

FIG. 8. The ionization energies E_{ion}, representing E_V of Si NWells embedded in SiO_2 or in Si_3N_4 as a function of d_{NWell}. Each point represents a different sample. The valence-band edge of bulk Si is shown as a reference. The error bars refer to standard deviations in thickness and in energy (see Sec. A and Ref. [26]).

known for bulk Si. Expressing these values in terms of ΔE_V, we obtain $\Delta E_V(d_{\mathrm{NWell}} = 11\text{--}20$ Å, SiO₂$) = -0.68$ eV and $\Delta E_V(d_{\mathrm{NWell}} = 11\text{--}20$ Å, Si₃N₄$) = +0.21$ eV, decreasing to $\Delta E_V(d_{\mathrm{NWell}} = 25 \pm 1$ Å, SiO₂$) = -0.65$ eV and $\Delta E_V(d_{\mathrm{NWell}} = 25 \pm 1$ Å, Si₃N₄$) = +0.09$ eV. The difference in E_V values for Si NWells embedded in SiO₂ versus Si₃N₄ thus undergoes a minor decrease from 0.89 eV for $d_{\mathrm{NWell}} = 11\text{--}15$ Å to 0.74 eV for $d_{\mathrm{NWell}} = 25 \pm 1$ Å. Since Si NWells have significantly lower fundamental gaps as compared to Si NCs (cf. Figs. 5 and 6), a pronounced *n*- or *p*-type charge-carrier preference arises from the above energy offsets for $d_{\mathrm{NWell}} \leq 28$ Å.

We plan to measure the conduction-band states of NWell samples along with UPS characterizations on the same samples, motivated by Zimina *et al.* [45], who characterized the E_C value of Si NCs embedded in SiO₂ for $d_{\mathrm{NC}} = 16\text{--}40$ Å by soft-x-ray emission spectroscopy (SXES). A *downshift of E_C up to 0.2 eV below the conduction-band edge E_C of bulk Si* has been obtained [45]. Conventional quantum physics strongly suggests E_C to be located a few 100 meV above the E_C value of bulk Si, which already includes contributions from excitonic binding and dielectric screening. The same work also noted that the interface of Si NCs is not abrupt but rather gradual, with suboxide shells in a thickness range of 3–5 Å. This value is likely underestimated, since similar superlattices of Si NCs with suboxide shells characterized by atom-probe tomography have been found to have suboxide shells of approximately 8 Å [9,46]. Such thicker suboxide shells will attenuate the ICT and thus ΔE due to the suboxide not having the full ΔE impact on dns-Si and, at the same time, working as an electrostatic buffer between the Si NC and the SiO₂. Since our NWell samples have plane interfaces and have not been processed by excess Si segregation from a suboxide [5], the interface thickness is on the order of 5 Å, as occurs in conventional *c*-Si oxidation [47]. Hence, it appears that higher-energy offsets ΔE_C and consequently ΔE_V exist for NWells as compared to Si NCs formed by segregation from Si-rich dielectrics [5,36].

To sum up, $E_V = E_{\mathrm{vac}} - 5.17$ eV $= E_V$(bulk Si) for NWells with $d_{\mathrm{NWell}} = 40\text{--}50$ Å in both SiO₂ and Si₃N₄. We take this value as the common baseline from which to count ΔE_V with decreasing d_{NWell} as per dielectric. For $d_{\mathrm{NWell}} = 30\text{--}40$ Å, a transition range exists with increasing ΔE_V between NWells in SiO₂ versus Si₃N₄. At $d_{\mathrm{NWell}} = 25 \pm 1$ Å, the respective E_V values are fully developed with $\Delta E_V \approx 0.74$ eV, although they still increase to approximately 0.9 eV for $d_{\mathrm{NWell}} = 11\text{--}15$ Å. Thus, a strong *n*- or *p*-type carrier preference exists for dns-Si in SiO₂/Si₃N₄, which can induce a *p-n* junction for $d_{\mathrm{NWell}} \leq 28$ Å [cf. Figs. 6(g)–6(i)]. Published characterization data on Si NCs prepared by segregation annealing from Si-rich SiO₂ [45] show *negative* ΔE_C values, resulting in $E_C \approx E_C$(bulk Si) $- 0.2$ eV. As the electronic quality and abruptness of the interface of Si NWells is notably superior to those of segregated Si NCs having warped and/or multi-faceted interfaces, the negative ΔE_C values of the NWells should be more pronounced in SXES measurements.

V. PROPOSED MECHANISM OF ENERGY OFFSET

With the quantitative theoretical and experimental data presented above, we propose a qualitative model for the energy offsets ΔE_V and ΔE_C induced by embedding in SiO₂ versus Si₃N₄. From there, we determine the impact length of ΔE_V and ΔE_C in dns-Si systems.

A. Basic principle

A brief look at some element-specific quantum-chemical parameters of O, N, and Si as listed in Table II is very helpful in explaining ΔE.

For O, the explanation of ΔE is fairly straightforward. With a high negative X and an ionicity of bond (IOB) to Si of approximately 53%, O localizes electronic charge from dns-Si, thereby increasing the binding energy of such electrons, which present the valence states of dns-Si with the lowest binding energy. As a consequence, E_V (dns-Si) is shifted further below E_{vac}. Since Si atoms have a reasonably high E_{ion} value, which counteracts electron removal, the ICT feeding into electron localization at O decreases from its saturation value (maximum positive ionization) after a few MLs of the dns-Si system. Eventually, the impact of the ICT due to O at the dns-Si interface vanishes, whereby E_V(dns-Si) $\rightarrow E_V$(bulk Si). The top graph of Fig. 9 illustrates this behavior.

The situation with N requires some broader considerations of its properties. Out of all of the chemical elements that are known to expose anionic properties (main groups IV–VII of the periodic table), N is the only element that possesses a *positive* electron affinity X, which means that turning N into a negative ion (a Lewis acid [42]) requires a significant activation energy. Therefore, N is very reluctant to accept a negative charge such as from dns-Si, which becomes even more prominent when compared to O. This

TABLE II. Fundamental properties of the chemical elements (ϵ) N, O, and Si: the ionization energy (E_{ion}), electron affinity (X), and electronegativity (EN), the ensuing IOB to Si, and the experimental values of the characteristic bond lengths [42].

ϵ	E_{ion}[a] (eV)	X (eV)	EN[b]	IOB (%)	d_{bond} to Si (Å)
N	14.53	+0.07	3.07	36	0.1743 (Si₃N₄)
O	13.36	−1.46	3.50	54	0.1626 (SiO₂)
Si	8.15	−2.08	1.74	0	0.2387 (bulk Si)[c]

[a]Refers to the first valence electron.
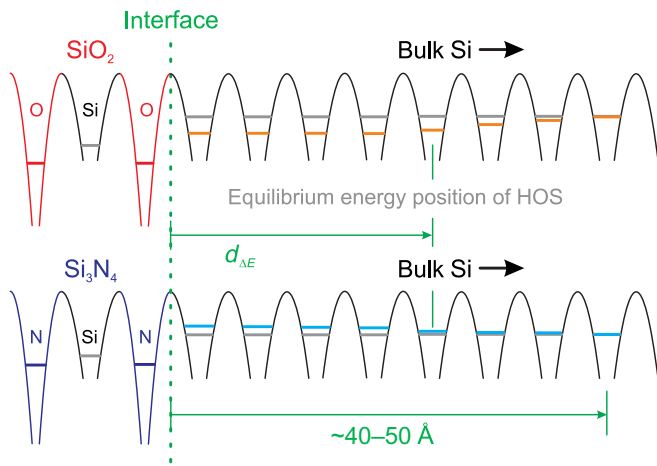[b]Values after Allred and Rochow.
[c]With a unit-cell length of 0.5431 nm [48].

FIG. 9. The principle of how the energy offset in dns-Si is induced on the quantum scale. The top graph shows the atomic potential at the SiO_2-Si interface and the bottom graph shows the situation at the Si_3N_4-Si interface. The gray valence levels refer to equilibrium positions in bulk Si. The impact length of the energy offset $d_{\Delta E}$ defines the distance from the interface at which ΔE leaves the saturation regime, as obtained from UPS measurements.

fact is well known from some basic chemical reactions, such as creating ammonia (NH_3) from the elements:

$$N_2 + 3H_2 \xrightarrow{650\,^{\circ}C, 300\,bar,\, Fe\,contact} 2NH_3 + 92.3\,kJ/mol,$$
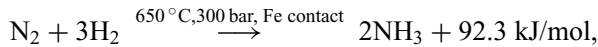
which requires a catalytic iron contact at 300 bar and 650 °C to trigger the above reaction, in a process known as Haber-Bosch synthesis [42]. In contrast, O reacts violently with H at room temperature at 1 bar (oxyhydrogen reaction) [42]:

$$O_2 + 2H_2 \longrightarrow 2H_2O + 572.0\,kJ/mol.$$
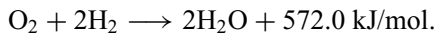
Considering Si, oxidation of Si surfaces to SiO_2 in elemental O_2 proceeds readily at room temperature and is promoted by the presence of H_2O. In contrast, the nitridation reaction requires the Si surfaces to be offered atomic and/or ionic N in a plasma several 100 °C above room temperature in order to achieve the reaction.

This uncommon behavior of N is at the heart of the energy offset: while N delocalizes the electrons of a dns-Si system at the top of its valence band, it does not localize such electrons but, rather, deflects them back into the dns-Si and the adjacent Si_3N_4. This delocalization results in a lower binding energy of these valence electrons. From Fig. 8, we also see that the delocalizing impact of N on E_V(dns-Si) does not show a strict saturation for $d_{NWell} \leq$ 25 Å, as is the case for SiO_2 embedding. This behavior has to be seen in the context of electron delocalization, which is more sensitive to environmental changes, such as an increase of the number of NWell Si atoms per N atom in

Si_3N_4. We can therefore state that ΔE generated by Si_3N_4 embedding is not as robust as ΔE due to SiO_2.

The partial deflection of delocalized electrons into the first couple of MLs of Si_3N_4 explains the stronger shift of E_{HOMO} and E_{LUMO} toward E_{vac} for $\langle 111 \rangle$-octahedral Si NCs in 1.5-ML versus 1-ML Si_3N_4 (cf. Fig. 5). The same consequence occurs when going from $\langle 111 \rangle$-octahedral to $\langle 001 \rangle$-cubic Si NCs, where the N_{IF}/N_{NC} ratio increases significantly. Furthermore, such behavior can clearly be seen for the frontier OMOs at approximants that feature a Si NC in Si_3N_4 plus a Si NC in SiO_2 [see Sec. B and Figs. 6(b), 6(e), and 6(h)]. The resulting shift of E_V(dns-Si) toward E_{vac} within the first few MLs of dns-Si is shown in the bottom graph of Fig. 9.

Figure 8 shows that $|\Delta E_V(SiO_2)| \approx 5.17$ eV $+ 2 \times |\Delta E_V(Si_3N_4)|$. This finding correlates qualitatively with the IOB of N versus O to Si. Other factors, such as the anion-to-Si ratio, positive $X(N)$ versus negative $X(O)$, the bond length, and the packing fraction in the dielectric, also have an influence on this ratio.

Since we intend to use ΔE for undoped p-n junctions, we consider it useful to define the impact length $d_{\Delta E}$ as the distance from the dns-Si interface to the point at which E_V leaves the saturated regime. This definition of $d_{\Delta E}$ provides the optimum impact for undoped p-n junctions, since the global energy gap of the dns-Si system decreases with its increasing size (see Fig. 10).

It is important to note that the effect we describe cannot be sufficiently explained by interface dipoles [49] manipulating the electronic structure, as reported for metal-semiconductor (Schottky) barriers, e.g., for GaAs [50] or Si [51]. Further progress in manipulating the electronic structure of Si surfaces has been obtained by diazonium ions with NO_2 versus NH_2 end groups accounting for an acceptor- and donorlike character, respectively [52]. Pseudo-metal-oxide-semiconductor
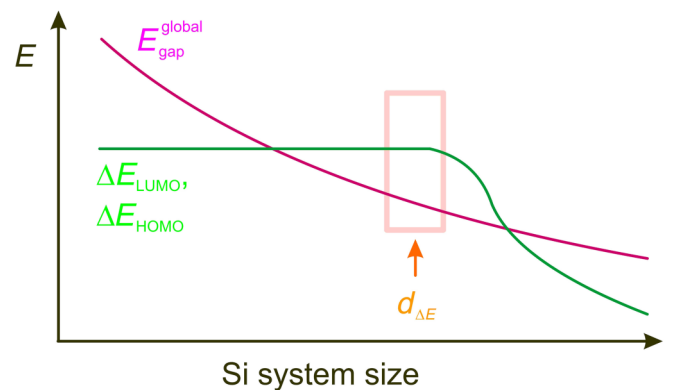

FIG. 10. A qualitative scheme to explain the dependence of the energy offset and the global energy gap as function of the dns-Si system size. The technological optimum for maximum n- or p-type carrier preference is shown by the semitransparent pink frame, defining $d_{\Delta E}$ as per the explanation in the text.

FETs (MOSFETs) with 1 ML of such functionalized molecules have been carefully processed in an inert atmosphere throughout, showing a significant shift in threshold voltage. As for metals, the electron work function of silver (Ag) surfaces has been manipulated by thio-hydrocarbons with methyl (CH_3-), NH_2-, or F-group-inducing interface dipole moments of $+2.24$, $+1.77$, and -1.69 Debye, respectively [53]. Qualitatively similar results have been obtained for gold (Au) and Ag coated with 1 self-assembled ML (SAM) of thio-hexadecanol ($HS\text{-}C_{16}H_{33}$) or perfluorinated thio-decanol ($HS\text{-}C_{10}H_{20}F$) [54].

More work on metal surfaces with physisorbed molecular species has been carried out for Fe, Ni, and Cu covered with acrylonitrile ($H_2C{=}CH{-}C{\equiv}N$) [55], where the push-back or pillow effect has been observed [56]. This effect changes the electronic structure of the metal by Pauli repulsion between the electronic population of the adsorbate and the Fermi sea [57] of the metal and has also been observed for physisorbed Xe [58], benzene (C_6H_6), and cyclohexane (C_6H_{12}) [59] on $(111)\,Cu$ and for more complex organic conjugated molecules on Au [60]. Full chemical bonding exists at SiO_2-Si and Si_3N_4-Si interfaces. Apart from degenerate doping, the electronic structure of Si does not allow for a Fermi sea. Electrons are strongly localized in bonds, in particular at the interface to SiO_2 or Si_3N_4, where the bond energy increases over the values for the bond Si—Si [61–63]. In contrast to full chemical bonding, the push-back or pillow effect induced by the adsorption of a molecular species would not be sufficient to induce a notable shift of the entire electronic structure of Si.

In accordance with interface dipole theory, the cumulative ionization of the Si NCs in the DFT calculations should differ considerably, as is apparent from the dipole moments for functionalized thio-hydrocarbons [53] mentioned above. However, this is not the case, as is evident from Figs. 4 and 7. Instead, the electronic charge between two embedded Si NCs of size 11, 15, or 19 Å (one in SiO_2 and the other in Si_3N_4; see Fig. 7) differs by only about 6%, which cannot account for a shift of the electronic structure by approximately 1.3 eV in DFT (Fig. 6) and by 0.9 eV at Si NWells in the experiments (Fig. 8). Unlike an interface dipole, which is defined by 1 ML, the total ionization of Si NCs shifts to higher (lower) values for SiO_2 (Si_3N_4) as a function of the number of embedding dielectric MLs [21] and saturates for approximately 3 dielectric MLs. Furthermore, N and O are both strong anions regarding Si, which should result in a similar trend for the shift of the electronic structure. This is clearly not the case: see Figs. 5 and 6 for theoretical and Fig. 8 for experimental data. Furthermore, neither of the dielectrics introduces additional states within the fundamental gap of the NCs, as would be the case for interface dipoles [49].

An increasing leakage of electron wave functions from Si into the respective dielectric due to quantum confinement with a shrinking Si system size (d_{NC}, d_{NWell}) would scale with $3/d_{NC}^2$ for NCs and with $1/d_{NWell}^2$ for NWells. In contrast to such hyperbolic behavior, we observe an almost steplike change of ΔE_V around $d_{NWell} \approx 35$ Å for SiO_2-embedded NWells. Due to the positive X of N and its lower IOB to Si, this behavior is less pronounced for Si_3N_4-embedded Si NWells (see Ref. [21] for additional UPS data). Nearly constant values for ΔE_{HOMO} and ΔE_{LUMO} corroborate this observation in DFT calculations for Si NCs with the same surface orientation (cf. Figs. 5 and 6), as the NC size in DFT does not reach into the region in which ΔE_{HOMO} and ΔE_{LUMO} leaves the saturated regime.

Our discussion strongly proposes that the main impact of SiO_2 and Si_3N_4 is due to the nature of the anion forming the dielectric, as per our explanation above.

B. Calculation of impact length of ΔE in dns-Si

From the measurements of $E_V(d_{NWell})$ by synchrotron UPS, we derive $d_{NWell} \approx 28$ Å as the saturation limit beyond which ΔE decreases significantly. NWells have two adjacent interfaces, which immediately yields $d_{\Delta E}(\text{bulk Si}) = 1/2 \times d_{NWell} \approx 14$ Å. This value presents the limit for the semi-infinite case, i.e., an interface to bulk Si. The volume element defining $d_{\Delta E}(\text{bulk Si})$ is a cubicle of height $d_{\Delta E}(\text{bulk Si})$, its width and length being defined by the smallest periodic unit in the respective direction. For NWells, we thus obtain $d_{\Delta E}(\text{Si NWell}) = 2 \times d_{\Delta E}(\text{bulk Si})$, arriving at the value obtained by synchrotron UPS (see the right-hand graph in Fig. 11).

As an approximation, NWires and NCs have warped interfaces that do not allow for a straightforward derivation of dV as is the case for NWells and bulk Si. Therefore, we derive the gauge for these dns-Si systems by
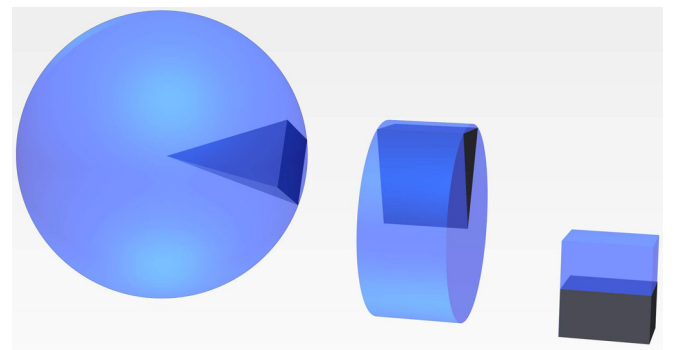
FIG. 11. An illustration of the volume elements dV used to describe the volume of NCs (left), NWires (center), and NWells (right). For NWires and NCs that have warped surfaces, the Riemann sum over all $dV(i)$ converges against the volume integral of the dns-Si system for $i \rightarrow \infty$, resulting in the base areas of dV converging to zero. The scaling of the system sizes matches the dV shape with constant volume and is thus 3:2:1 from left to right.

simple geometric arguments of volume integration via Riemann's sums [64]. For NWires, we cut out a slab that presents the smallest periodic unit along the NWire axis. This slab is then filled with volume elements $dV(i)$, representing the Riemann sum $\sum_i dV$ of the slab volume. For NWires, these $dV(i)$ are wedges (see center graph in Fig. 11). With $i \to \infty$, we achieve the transition from the Riemann sum to the volume integral, resulting in an infinite number of wedges with vanishing base area. With equal base areas, the volume of a wedge equals the volume of a cubicle if the height of the wedge is twice the height of the cubicle. Consequently, the impact length of ΔE doubles when going from NWells to NWires, resulting in $d_{\Delta E}(\text{Si NWire}) = 2 \times d_{\Delta E}(\text{Si NWell})$. For NCs, it is straightforward that we get pyramids as volume elements dV (see the left-hand graph in Fig. 11). With the same base area, a pyramid has the same volume as a cubicle if its height is 3 times the height of the cubicle. Accordingly, we obtain $d_{\Delta E}(\text{Si NC}) = 3 \times d_{\Delta E}(\text{Si NWell})$. Summarizing all dV definitions, we obtain $d_{\Delta E}$ scaling with bulk Si:NWell:NWire:NC like 1:2:4:6. With $d_{\Delta E}(\text{Si NWell}) \approx 28$ Å, we obtain $d_{\Delta E}(\text{Si NWire}) \approx 56$ Å and $d_{\Delta E}(\text{Si NC}) \approx 84$ Å.

In real systems, the rise in $d_{\Delta E}$ with decreasing dimensionality of the dns-Si system should be sublinear, originating from a higher defect density due to warped interfaces, which also has to be controlled by ΔE. We can account for this effect by exploiting the fact that the fundamental gaps E_{gap} of Si NCs are significantly larger for Si_3N_4 embedding compared to SiO_2 embedding if such NCs are small enough [32,33]. Experimental data show the E_{gap} of both embeddings to converge at $d_{\text{NC}} \approx 56$ Å [65]. Assuming a reduction factor per reduced dimension D and using $d_{\Delta E}(\text{Si NC}) = D^2 \times 4 \times d_{\Delta E}(\text{Si NWell})$, we arrive at $D \approx 1/\sqrt{2}$, yielding $d_{\Delta E}(\text{Si NWire}) \approx 40$ Å and $d_{\Delta E}(\text{Si NC}) \approx 56$ Å, below which ΔE is saturated.

VI. CONCLUSIONS

We present a detailed quantitative study of the considerable energy offsets of frontier electronic states as a fundamental effect arising from deeply nanoscale silicon (dns-Si) volumes when embedded and/or coated in SiO_2 versus Si_3N_4.

Using DFT, we investigate single Si NCs as a function of the interface orientation and thickness of the embedding SiO_2 versus Si_3N_4 up to $d_{\text{NC}} = 26$ Å. We find that E_{HOMO} and E_{LUMO} have little dependence on the NC size in the range considered, showing a strong offset due to 1.5-ML SiO_2 versus Si_3N_4 embedding of $\Delta E_{\text{HOMO}} \approx 1.75$ eV and $\Delta E_{\text{LUMO}} \approx 1.93$ eV. These offsets push E_{HOMO} and E_{LUMO} of SiO_2-embedded Si NCs further below E_{vac}, while shifting E_{HOMO} and E_{LUMO} of Si_3N_4-embedded Si NCs toward E_{vac}. Extending the embedding in $\text{SiO}_2/\text{Si}_3\text{N}_4$ beyond 1 ML and, in particular, increasing the ratio of

interface bonds per NC atom $N_{\text{IF}}/N_{\text{NC}}$ by going from ⟨111⟩-octahedral to ⟨001⟩-cubic NCs increases ΔE further. As an ultimate theoretical test, we compute approximants featuring two Si NCs of up to size 18.5 Å, one each embedded in SiO_2 and Si_3N_4, respectively, confirming ΔE within one system.

We characterize 14 samples, each featuring one Si NWell of $d_{\text{NWell}} = 11$–50 Å embedded in SiO_2 or in Si_3N_4, by long-term synchrotron UPS to measure the energy of the top valence-band states E_V. For $d_{\text{NWell}} \lesssim 28$ Å, we obtain $\Delta E_V \approx 0.9$ to 0.74 eV for SiO_2 versus Si_3N_4 embedding. After a transition range at $d_{\text{NWell}} \approx 30$–40 Å, the Si NWells in both embeddings converge to $E_V = E_V(\text{bulk Si})$. Zimina *et al.* [45] found the energy of the lowest unoccupied states at $E_C \approx E_C(\text{bulk Si}) - 0.2$ eV for SiO_2-embedded Si NCs, attractive interactions such as the exciton binding energy and screening already being included in this value. This finding is consistent with our results on E_V of thin Si NWells in SiO_2.

Investigating the quantum chemistry of O and N with respect to Si, we propose a model for ΔE. The uncommon situation of N as the only anionic element with an electron affinity $X > 0$ eV and yet a fairly high electronegativity EN inducing a strong polar bond to Si is one cornerstone of the effect. While N delocalizes valence electrons from dns-Si, it does *not* localize such electrons but deflects them back into the dns-Si or the surrounding Si_3N_4, as is also evident from the frontier-OMO density plots in the DFT calculations spreading well into Si_3N_4. As a consequence, such delocalized NWell valence-band states have a lower binding energy, which is equivalent to an upshift of $E_V(\text{NWell})$ toward E_{vac}. As expected, the strong conventional anionic nature of O results in strong localization of valence electrons from dns-Si at O in SiO_2 and an associated downshift of $E_V(\text{NWell})$ below E_{vac}.

Using a straightforward geometrical Riemann model, we calculate the impact length $l_{\Delta E}$ up to which ΔE governs the electronic structure of dns-Si to scale 1:2:4:6 for bulk Si:NWell:NWire:NC. With $l_{\Delta E}(\text{NWell}) \approx 28$ Å, we thus arrive at $l_{\Delta E}(\text{NWire}) \approx 56$ Å and $l_{\Delta E}(\text{NC}) \approx 84$ Å. The latter two dns-Si structures have warped interfaces, which are more prone to defects; experimental data from the literature on the difference in the fundamental gap of Si NCs embedded in SiO_2 versus Si_3N_4 yield $l_{\Delta E}(\text{NC}) \approx 56$ Å. We introduce a dimensionality factor D per reduced dimension (NWells $\xrightarrow{\times D}$ NWires $\xrightarrow{\times D}$ NCs) of $D \approx 1/\sqrt{2}$, accounting for an increased number of defects at warped interfaces, yielding $l_{\Delta E}(\text{NWire}) \approx 40$ Å and matching $l_{\Delta E}(\text{NC}) \approx 56$ Å.

The ΔE value in dns-Si due to coating with or embedding in SiO_2 (Si_3N_4) induces a strong preference for electrons (holes) and thus for *n*-type (*p*-type) Si. Applying such preferences to dns-Si would eliminate all issues of impurity doping—out-diffusion, clustering, self-purification, ionization at room and cryogenic

temperatures, and inelastic carrier scattering—and potentially extend device miniaturization down to the minimum size of Si crystallites, of approximately 1.5 nm [20], along with much reduced bias voltages and heat loss.

ACKNOWLEDGMENTS

APPENDIX: EVALUATION OF UPS DATA

In our recent publication, we discussed the calibration of UPS scans and data extraction by local fitting of amorphous backgrounds using Si_3N_4-embedded Si NWells of thicknesses 17 and 27 Å in considerable detail [26].

Here, we just focus on one SiO_2- and one Si_3N_4-embedded sample for determining the valence-band edge, its standard deviation over energy, and associated local background fitting per scan to explain the principle. We further explain several plausibility tests as an additional means of arriving at the correct data. As examples, we pick UPS scans of sample N-15-D, comprising a 15-Å Si NWell in Si_3N_4, and of sample SOO-15, comprising a 12-Å Si NWell in SiO_2. Both scans have the lowest signal-to-noise ratio (SNR) against the background due to secondary electrons and SiO_2/Si_3N_4. This circumstance predestines both samples to demonstrate the UPS data-filtering algorithm to obtain the valence-band edge of buried Si NWells. Figure 12 shows the global UPS scans of both samples, which are measured during beam time 1 at the BaDElPh beam line at the Elettra Sincrotrone Trieste, Italy (cf. Fig. 8). The common parameters are the UV photon energy of $h\nu = 8.7$ eV and the background counts-per-second value of 1950, which is derived in the E_{kin} interval of $[h\nu; h\nu - 0.5]$ eV = [8.7; 8.2] eV. This background counts-per-second value, derived from the Si reference, serves as a calibration standard and thus sets the counts-per-second intercept for all UPS scans (see Ref. [26] for details).

Below, we describe the algorithm to determine the valence-band edge of a Si NWell embedded in Si_3N_4 or
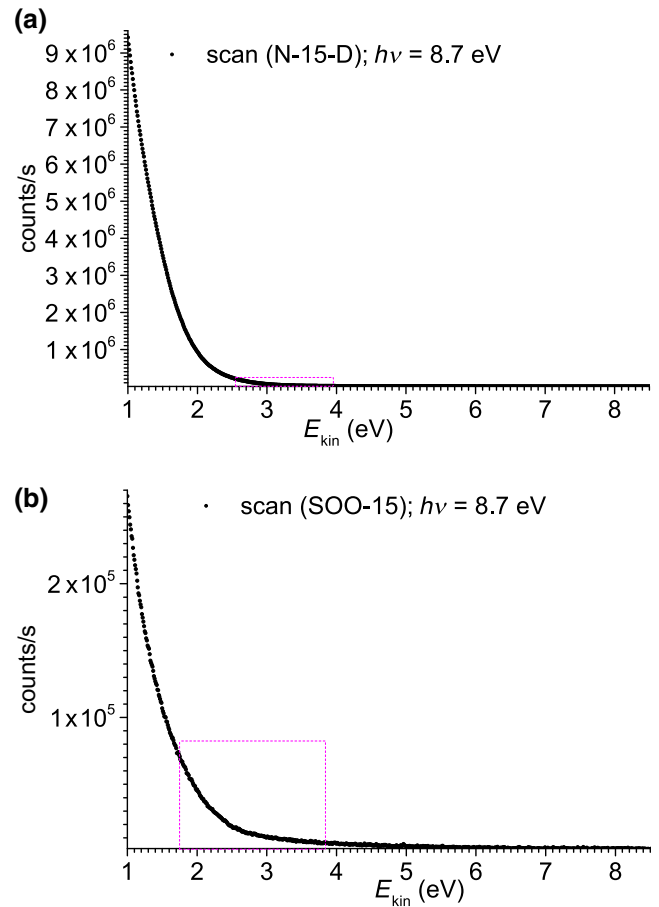

FIG. 12.   The complete UPS scans of samples (a) N-15-D and (b) SOO-15, shown with the respective regions of interest marked as magenta frames. The photoexcitation energy is $h\nu = 8.7$ eV. Note the different counts-per-second scales on the abscissas.

SiO_2. We begin by checking the UPS scan for regions of reasonably linear values with ≥ 15 points, equivalent to an E_{kin} range of 0.15 eV. The following steps are applied to every linear region found. We assign the number of points forming the linear region to N_{pts}. We then run a linear fit over the edge region and calculate its sum of residual squares $\sum [\text{data}(E_{kin}) - \text{fit}(E_{kin})]^2$ and its average counts-per-second value $= 1/N_{pts} \sum \text{data}(E_{kin})$. With these three values, we can calculate the normalized sum of residual squares which takes into account the signal intensity and length of the linear region: normalized sum of residual squares = sum of residual squares $/[N_{pts} \times$ average counts-per-second value] $= \left(\sum [\text{data}(E_{kin}) - \text{fit}(E_{kin})]^2 \right) / \sum \text{data}(E_{kin})$. The linear region with the minimum normalized sum of residual squares is the edge of the Si NWell, subject to passing a number of plausibility tests outlined below. The intercept of the linear fit provides the E_{kin} value that yields the top of the valence band of the Si NWell via $E_V = h\nu$
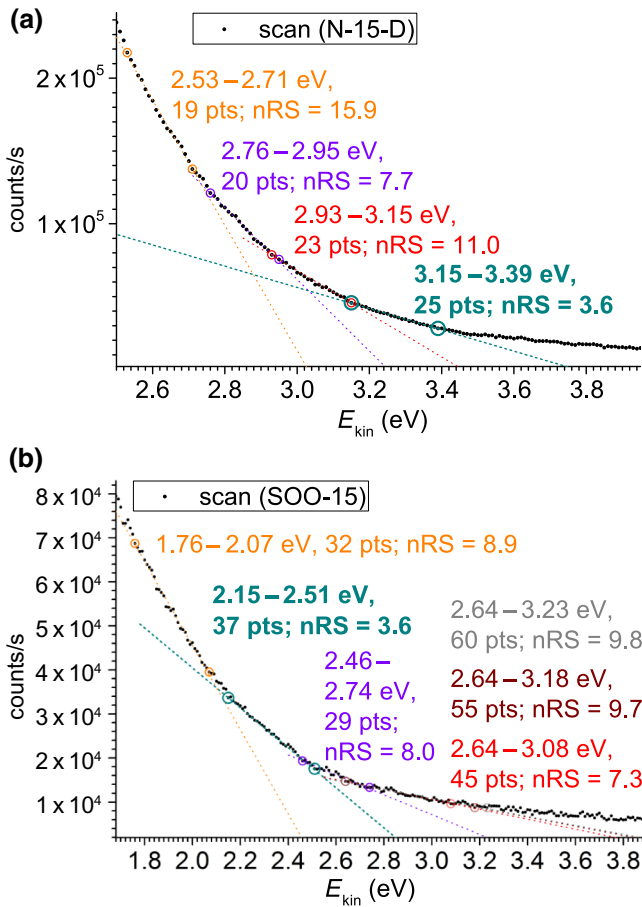
(a)

(b)

FIG. 13.   The range of interest of the UPS scans of samples (a) N-15-D and (b) SOO-15, shown with all linear regions found as per the definition in the text. The ranges of E_{kin}, N_{pts}, and the normalized sum of residual squares are shown per linear fit. The bold-printed parameters in dark cyan and the associated fit are the valence-band edge of the embedded Si NWell.

(a)

(b)

FIG. 14.   The difference between the UPS signal and the linear fit to the edge region, shown in the ± 1 E_{kin}(edge) interval for samples (a) N-15-D and (b) SOO-15; see the text for details. The lower graphs show the edge region, including linear fits to local point groups with an associated alignment. These fits are used for estimating the standard deviation of the valence-band edge over E_{kin}.

$- E_{kin}$(intercept). Figure 13 shows the range of interest per UPS scan with all of the linear regions detected.

Next, we calculate the standard deviation $\sigma(E_{kin})$, using the difference between the UPS signal and its linear fit (cf. Fig. 14). Within the edge region, we group points with associated alignment. For these, we calculate local fits and determine their intercepts (cf. Fig. 15). The resulting E_{kin} values are used together with the value of the linear fit to the entire edge region to determine $\sigma(E_{kin}) = \sqrt{1/n \sum_{i=1}^{n} [\overline{E}_{kin} - E_{kin}(i)]^2}$ [64] and are shown as error bars of E_{ion} in Fig. 8. We note that—as the samples are measured at $T = 300$ K—the minimum error bar for E_{kin}, E_{ion} is set to $k_B T = 0.026$ eV.

Since the algorithm on its own may yield a couple of possible solutions, we carry out additional plausibility tests. One of them is a combination of the smoothed UPS signal, an associated background fit, and the interpolation of the resulting differential signal. First, we take
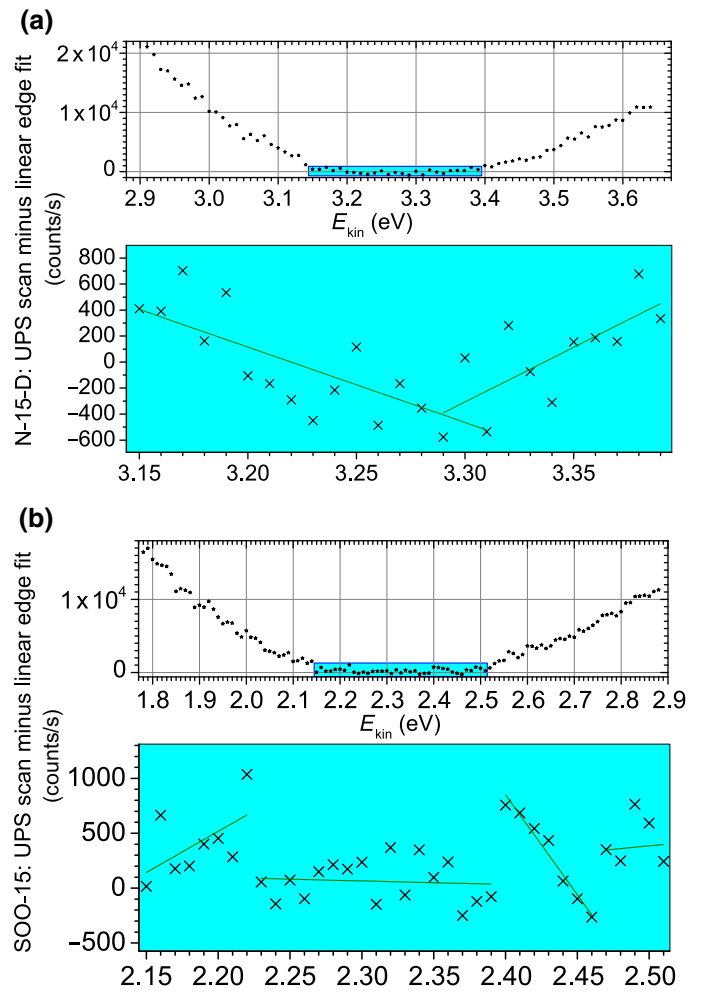
the UPS data of the edge region plus one energy range as defined by the edge regions above and below the edge (e.g., N-15-D has an edge from $E_{kin} = 3.15$ to 3.39 eV [25 points], so we now pick UPS data from 2.90 to 3.64 eV [$25 + 25 + 25 = 75$ points]). To this data set, we apply a Sawitzky-Golay smoothing [66] over six points with a second-order polynomial as an effective means of *removing single-point runaways without altering the spectral information* (cf. Fig. 15). Thereby, we get less noisy UPS data in the range of interest. This smoothed UPS data is used for a background fit, whereby we exclude the actual edge region ($E_{kin} = 3.15$ to 3.39 eV [25 points] for sample N-15-D). Since higher-order polynomials can be interpreted as the finite Taylor series of an exponential function, $\exp(x) = \sum_{i}^{\infty} [x^i / i!]$, we choose polynomials to fit the background and use the signal-calibration intercept
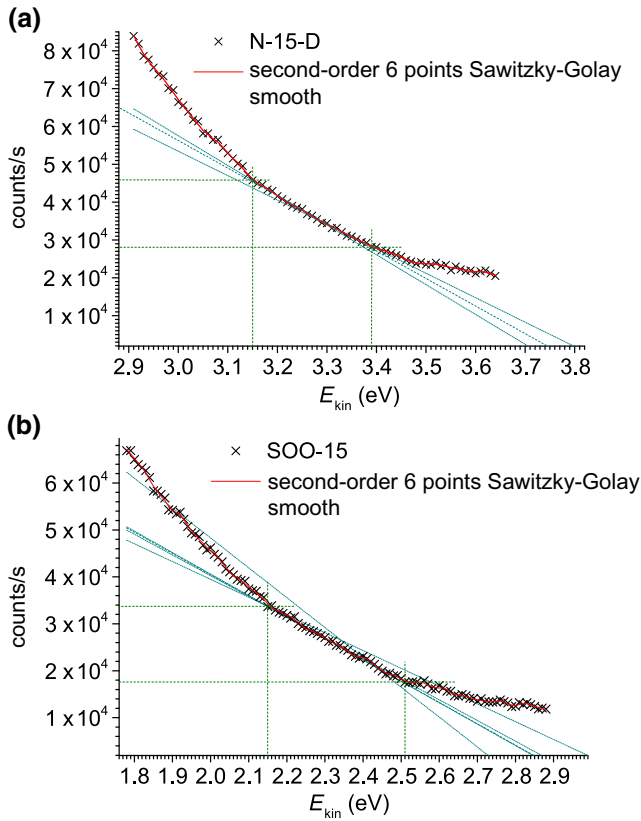
FIG. 15. The UPS scan and its Sawitzky-Golay smoothed version of the edge-region $\pm 1\, E_{kin}$(edge) interval around it, shown for samples (a) N-15-D and (b) SOO-15. The thick dashed lines show the valence-band edge of the Si NWell and the thin dashed lines show local linear fits to point groups showing local alignment within the edge region. The latter are used to calculate the standard deviation of the edge over E_{kin} and thus E_V. The green dashed lines show the counts per second and the E_{kin} limits of the edge region.

FIG. 16. The Sawitzky-Golay smoothed data of the UPS scan in the $\pm 1\, E_{kin}$(edge) interval, shown for samples (a) N-15-D and (b) SOO-15 (see text for details). The red line shows the polynomial fit to the smoothed UPS data, which present the local surroundings of the edge region, serving as a local background with a lower SNR.

of 1950 counts/s as the coefficient for $i = 0$ (see Fig. 16). While the coefficients of the x^i decrease from $i > 1$, qualitatively agreeing with the Taylor series of an exponential function, there is still some degree of freedom to adapt to local deviations. These are evident even after Sawitzky-Golay smoothing (cf. Figs. 13 and 16). The exponential behavior of the signal background originates from the Urbach tails of the amorphous dielectric [67], with additional contributions due to inelastic electron scattering.

We now can calculate the difference between the smoothed UPS signal and the background fit where the edge region shows up above the noise (cf. Fig. 17). Due to the finite error in background fitting, there are local deviations of the fit from data points in the local environment of the edge region that cannot be accounted for. As a consequence, the first few points outside the edge region tend to be further away from the background fit, which can cause a dumping of the first few data points within the edge region. We also note that the fit does not account for an
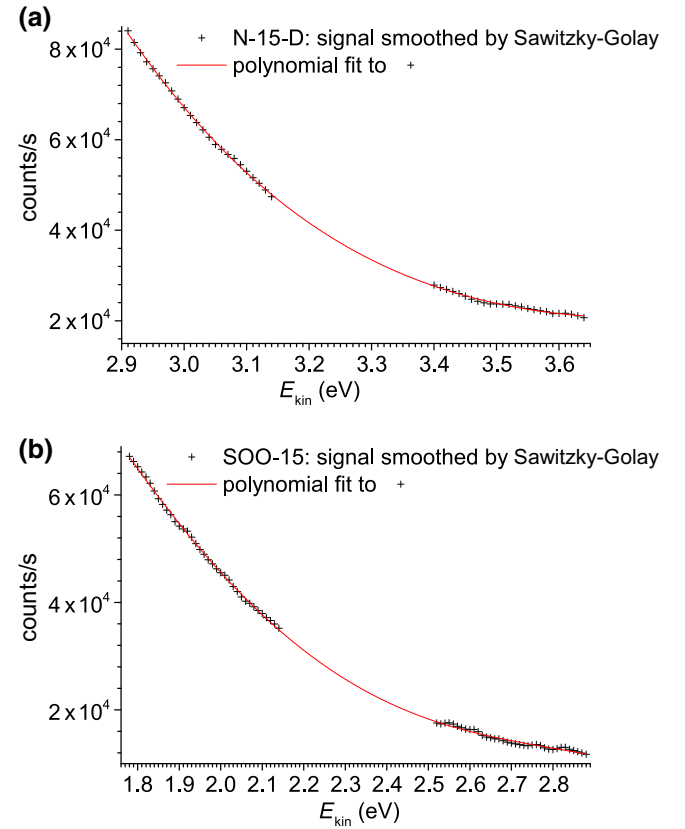
irregular rather rapid low-amplitude oscillation of the UPS signal. Hence, we have to look for positive signals—the edge signal occurs on top of the background—on a prolonged energy scale, ruling out rapid oscillations. To this end, we run a cubic B-spline interpolation [64] on the differential signal, which minimizes the oscillatory behavior (cf. Fig. 17).

Another plausibility test is given by measuring NWell samples with different d_{NWell} values, with a dielectric top layer of possibly constant thickness. Assuming that the dielectric top layer and its interface to the NWell have exactly the same thickness for all samples per dielectric type and that all measurement conditions are constant, the signal intensity (counts per second) of the NWell is related to the layer thickness of the top dielectric layer d_{diel}^{top} and d_{NWell} via counts/s$(d_{NWell}) \propto \exp(-d_{diel}^{top}/\lambda_{IMFP})[1 - \exp(-d_{NWell}/\lambda_{IMFP})]$, reducing to counts/s$(d_{NWell}) \propto 1 - \exp(-d_{NWell}/\lambda_{IMFP})$ for $d_{diel}^{top} = $ const. The average inelastic mean free path of excited electrons is presented by λ_{IMFP}. For brevity, we introduce one value for the Si NWell and the respective dielectric. It is interesting to
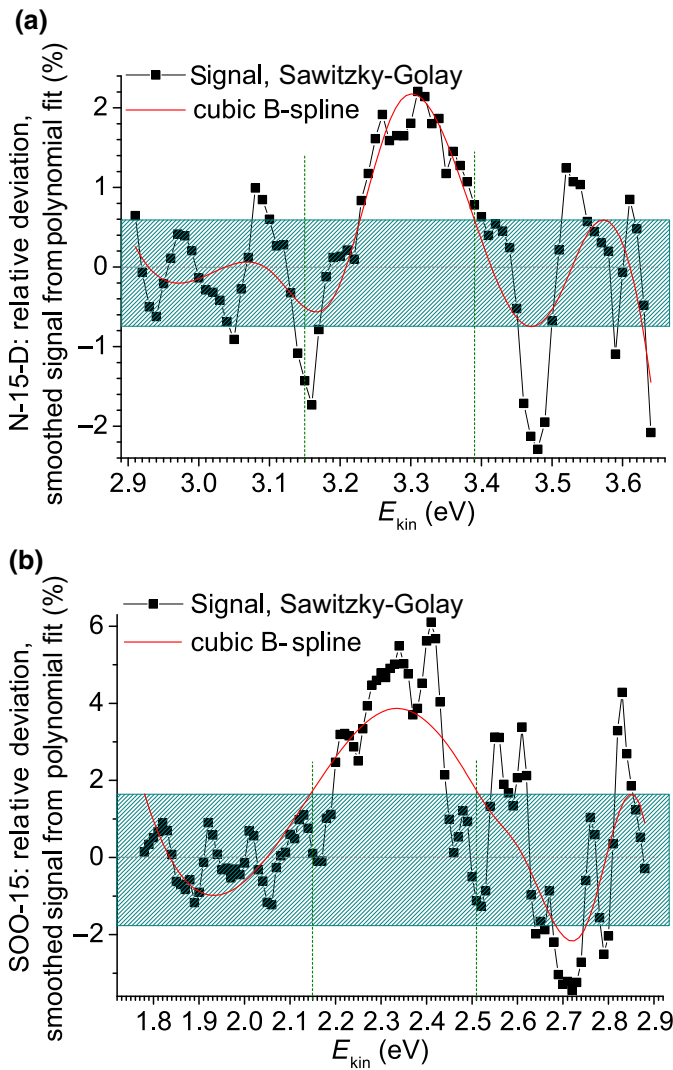
(a)

(b)

FIG. 17.   The relative (rel.) difference between the Sawitzky-Golay smoothed UPS scan and the background fit (cf. Fig. 16) of edge-region ± 1 E_{kin}(edge) interval around it, shown together with a cubic B-spline interpolation to minimize noise, for samples (a) N-15-D and (b) SOO-15. The green dashed lines show the E_{kin} limits of the edge region. The hashed dark-cyan area is a guide to the noise limit.

note that λ_{IMFP} has been overestimated in UPS for several compounds [68,69], since its widely used empirical description by Seah and Dench [70] was derived for many chemical elements and compounds for $h\nu \geq 150$ eV but only for three compound materials using $h\nu \leq 40$ eV. In a perfect world, we should see a counts-per-second value that increases asymptotically with d_{NWell}. In reality, minor thickness deviations, in particular, of the top dielectric layer will soften this asymptotic behavior into a counts-per-second value that is monotonically increasing with d_{NWell} (cf. Fig. 18).

As for the UPS signal quality, we can state that the SNR is higher for Si NWells embedded in SiO_2 versus
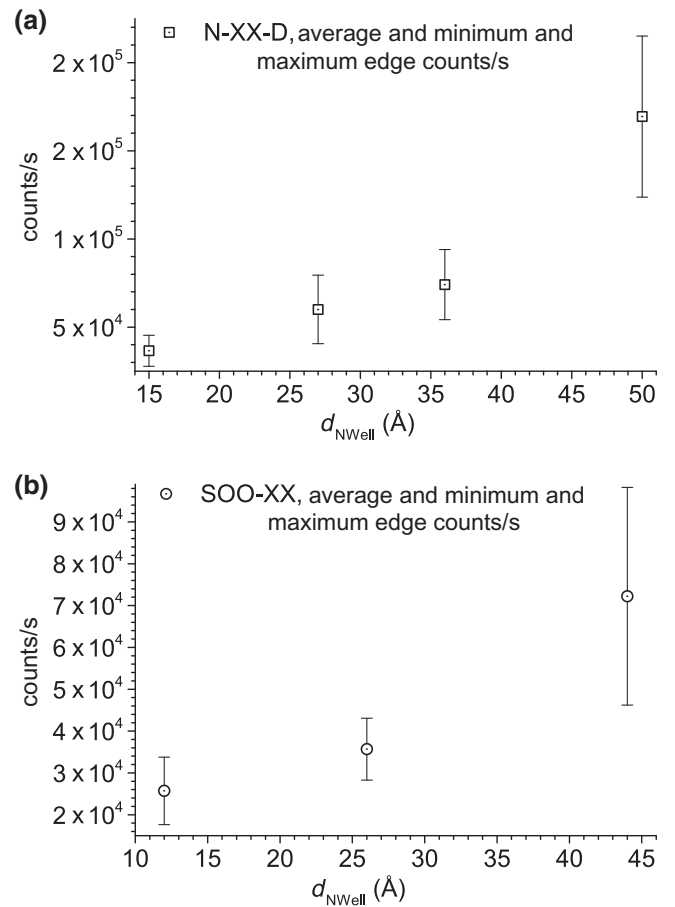

(a)

(b)

FIG. 18.   The average value of the counts per second of the edge region per sample of beam time 1 (cf. Fig. 8 for results), for Si NWells embedded in (a) Si_3N_4 and (b) SiO_2. The error bars show the minimum and maximum counts-per-second values per edge region.

Si_3N_4. This finding may come as a surprise, as the average counts per second per edge region are higher for NWells embedded in Si_3N_4 versus SiO_2. However, the difference in valence-band top energies is E_V(bulk Si) − E_V(Si_3N_4) = 1.78–1.88 eV [26,71] and E_V(bulk Si) − E_V(SiO_2) = 4.53–4.54 eV [26,71]. As a consequence, the Urbach tails of the amorphous Si_3N_4 layers deliver a significantly higher contribution to the UPS signal as opposed to SiO_2 (cf. Fig. 12). Furthermore, the packing fraction of Si_3N_4 and the density of electronic defects is notably higher as compared to SiO_2. This finding is also reflected in the greater range of the valence-band offset from Si_3N_4 to bulk Si of approximately 0.1 eV, as opposed to the value from SiO_2 to bulk Si (0.01 eV).

[1] G. L. Pearson and J. Bardeen, Electrical properties of pure silicon and silicon alloys containing boron and phosphorus, Phys. Rev. **17**, 865 (1949).

[2] S. Koelling, O. Richard, H. Bender, M. Uematsu, A. Schulze, G. Zschaetzsch, M. Gilbert, and W. Vandervorst, Direct imaging of 3D atomic-scale dopant-defect clustering processes in ion-implanted silicon, Nano Lett. **13,** 2458 (2013).

[3] A. K. Kambham, A. Kumar, A. Florakis, and W. Vandervorst, Three-dimensional doping and diffusion in nano scaled devices as studied by atom probe tomography, Nanotechnology **24,** 275705 (2013).

[4] R. Duffy, A. Ricchio, R. Murphy, G. Maxwell, R. Murphy, G. Piaszenski, N. Petkov, A. Hydes, D. O'Connell, C. Lyons, N. Kennedy, B. Sheehan, M. Schmidt, F. Crupi, J. D. Holmes, P. K. Hurley, J. Connolly, C. Hatem, and B. Long, Diagnosis of phosphorus monolayer doping in silicon based on nanowire electrical characterisation, J. Appl. Phys. **123,** 125701 (2018).

[5] J. Heitmann, F. Müller, M. Zacharias, and U. Gösele, Silicon nanocrystals: Size matters, Adv. Mater. **17,** 795 (2005).

[6] Gustavo M. Dalpian and James R. Chelikowsky, Self-Purification in Semiconductor Nanocrystals, Phys. Rev. Lett. **96,** 226802 (2006).

[7] A. R. Stegner, R. N. Pereira, R. Lechner, K. Klein, H. Wiggers, M. Stutzmann, and M. S. Brandt, Doping efficiency in freestanding silicon nanocrystals from the gas phase: Phosphorus incorporation and defect-induced compensation, Phys. Rev. B **80,** 165326 (2009).

[8] T.-L. Chan, Murilo L. Tiago, Efthimios Kaxiras, and James R. Chelikowsky, Size limits on doping phosphorus into silicon nanocrystals, Nano Lett. **8,** 596 (2008).

[9] D. König, S. Gutsch, H. Gnaser, M. Wahl, M. Kopnarski, J. Göttlicher, R. Steininger, M. Zacharias, and D. Hiller, Location and electronic nature of phosphorus in the Si nanocrystal-SiO$_2$ system, Sci. Rep. **5,** 09702 (2015).

[10] R. N. Pereira, A. J. Almeida, A. R. Stegner, M. S. Brandt, and H. Wiggers, Exchange-Coupled Donor Dimers in Nanocrystal Quantum Dots, Phys. Rev. Lett. **108,** 126806 (2012).

[11] D. Hiller, J. López-Vidrier, S. Gutsch, M. Zacharias, M. Wahl, W. Bock, A. Brodyanski, M. Kopnarski, K. Nomoto, J. Valenta, and Dirk König, Boron-incorporating silicon nanocrystals embedded in SiO$_2$: Absence of free carriers vs. b-induced defects, Sci. Rep. **7,** 8337 (2017).

[12] D. Hiller, J. López-Vidrier, K. Nomoto, M. Wahl, W. Bock, T. Chlouba, F. Trojànek, S. Gutsch, M. Zacharias, D. König, P. Malý, and M. Kopnarski, Absence of free carriers in silicon nanocrystals grown from phosphorus- and boron-doped silicon-rich oxide and oxynitride, Beilstein J. Nanotech. **9,** 1501 (2018).

[13] WikiChip website (2019), https://en.wikichip.org/wiki/WikiChip, see to technology nodes on right panel on the webpage (October 9, 2019).

[14] R. Dingle, H. L. Störmer, A. C. Gossard, and W. Wiegmann, Electron mobilities in modulation-doped semiconductor heterojunction superlattices, Appl. Phys. Lett. **33,** 665 (1978).

[15] D. König, D. Hiller, S. Gutsch, M. Zacharias, and S. Smith, Modulation doping of silicon using aluminium-induced acceptor states in silicon dioxide, Sci. Rep. **7,** 46703 (2017).

[16] D. Hiller, J. Göttlicher, R. Steininger, T. Huthwelker, J. Julin, F. Munnik, M. Wahl, W. Bock, B. Schoenaers, A. Stesmans, and D. König, Structural properties of Al-O monolayer stacks in SiO$_2$ and the maximization of their negative fixed charge density on Si, ACS Appl. Mat. Interfaces **10,** 30495 (2018).

[17] D. König, D. Hiller, and S. Smith, SiO$_2$ Modulation Doping for Si: Acceptor Candidates, Phys. Rev. Appl. **10,** 054034 (2018).

[18] D. König and J. Rudd, Formation of Si or Ge nanodots in Si$_3$N$_4$ with in-situ donor modulation doping of adjacent barrier material, AIP Adv. **3,** 012109 (2013).

[19] C.-C. Liu, E. Franke, Y. Mignot, R. Xie, C. Wing Yeung, J. Zhang, C. Chi, C. Zhang, R. Farrell, K. Lai, H. Tsai, N. Felix, and D. Corliss, Directed self-assembly of block copolymers for 7 nanometre FinFET technology and beyond, Nat. Electron. **1,** 562 (2018).

[20] S. Schuppler, S. L. Friedman, M. A. Marcus, D. L. Adler, Y. H. Xie, F. M. Ross, T. D. Harris, W. L. Brown, Y. J. Chabal, L. E. Brus, and P. H. Citrin, Dimensions of Luminescent Oxidized and Porous Silicon Structures, Phys. Rev. Lett. **72,** 2648 (1994).

[21] D. König, D. Hiller, N. Wilck, B. Berghoff, M. Müller, S. Thakur, G. Di Santo, L. Petaccia, J. Mayer, S. Smith, and J. Knoch, Intrinsic ultra-small nanoscale silicon turns n-/p-type with SiO$_2$/Si$_3$N$_4$-Coating, Beilstein J. Nanotech. **9,** 2255 (2018).

[22] C. N. Berglund and W. E. Spicer, Photoemission studies of copper and silver: Theory, Phys. Rev. **136,** A1030 (1964).

[23] C. N. Berglund and W. E. Spicer, Photoemission studies of copper and silver: Experiment, Phys. Rev. **136,** A1044 (1999).

[24] F. Reinert and S. Hüfner, Band offsets for ultrathin SiO$_2$ and Si$_3$N$_4$ films on Si(111) and Si(100) from photoemission spectroscopy, New J. Phys. **7,** 97 (2005).

[25] S. Suga and A. Sekiyama, *Photoelectron Spectroscopy*, Springer Series in Optical Sciences Vol. 176 (Springer, Berlin, 2014).

[26] D. König, D. Hiller, N. Wilck, B. Berghoff, M. Müller, S. Thakur, G. Di Santo, L. Petaccia, J. Mayer, S. Smith, and J. Knoch, Supporting information for intrinsic ultra-small nanoscale silicon turns n-/p-type with SiO$_2$/Si$_3$N$_4$-coating, Beilstein J. Nanotech. **9,** 2255 (2019), https://www.beilstein-journals.org/bjnano/content/supplementary/2190-4286-9-210-S1.pdf (accessed October 9, 2019).

[27] Gaussian09, *Revision D.01*, edited by M. J. Frisch *et. al.* (Gaussian, Inc., Wallingford, CT, 2010).

[28] M. S. Gordon, J. S. Binkley, J. A. Pople, W. J. Pietro, and W. J. Hehre, Self-consistent molecular orbital methods. 22. Small split-valence basis sets for second-row elements, J. Am. Chem. Soc. **104,** 2797 (1982).

[29] A. D. Becke, Density-functional exchange-energy approximation with correct asymptotic behaviour, Phys. Rev. A **38,** 3098 (1988).

[30] C. Lee, W. Yang, and R. G. Parr, Development of the Colle-Salvetti correlation-energy formula into a functional of the electron density, Phys. Rev. B **37,** 785 (1988).

[31] M. M. Francl, W. J. Pietro, W. J. Hehre, J. S. Binkley, D. J. DeFrees, J. A. Pople, and M. S. Gordon, Self-consistent

molecular orbital methods. 23. A polarization-type basis set for 2nd-row elements, J. Chem. Phys. **77,** 3654 (1982).

[32] D. König, J. Rudd, M. A. Green, and G. Conibeer, Role of the interface for the electronic structure of silicon quantum dots, Phys. Rev. B **78,** 035339 (2008).

[33] D. König, D. Hiller, S. Gutsch, and M. Zacharias, Energy offset between silicon quantum structures: Interface impact of embedding dielectrics as doping alternative, Adv. Mater. Interfaces **1,** 1400359 (2014).

[34] F. Rissner, D. A. Egger, A. Natan, T. Körzdörfer, S. Kümmel, L. Kronik, and E. Zojer, Collectively induced quantum-confined Stark effect in monolayers of molecules consisting of polar repeating units, J. Am. Chem. Soc. **133,** 18634 (2011).

[35] R. Dennington, T. Keith, and J. Millam, GaussView 5.0.8 (2009), semichem Inc., Shawnee Mission KS.

[36] D. Hiller, A. Zelenina, S. Gutsch, S. A. Dyakov, L. Lòpez-Conesa, J. Lòpez-Vidrier, S. Estradé, F. Peiró, B. Garrido, J. Valenta, M. Koínek, F. Trojánek, P. Malý, M. Schnabel, C. Weiss, S. Janz, and M. Zacharias, Absence of quantum confinement effects in the photoluminescence of Si_3N_4-embedded Si nanocrystals, J. Appl. Phys. **115,** 204301 (2014).

[37] L. Petaccia, P. Vilmercati, S. Goronikov, M. Barnaba, A. Bianco, D. Cocco, C. Masciovecchio, and A. Goldoni, BaDElPh: A 4 m normal incidence monochomator beam-line at Elettra, Nucl. Instr. Meth. Phys. Res. A **606,** 780 (2009).

[38] A. Thust, J. Barthel, and K. Tillmann, FEI Titan 80-300 TEM, Journal of Large-Scale Research Facilities (JLSRF) **2,** A41 (2016), doi:10.17815/jlsrf-2-66).

[39] D. König, Number series of atoms, interatomic bonds and interface bonds defining zinc-blende nanocrystals as function of size, shape and surface orientation: Analytic tools to interpret solid state spectroscopy data, AIP Adv. **6,** 085306 (2016).

[40] D. König and S. C. Smith, Analytic metrology of nanowires I: Regular cross sections for zincblende- and diamond-lattices, Acta Cryst. B **75,** 788 (2019).

[41] P. J. Hesketh, C. Ju, S. Gowda, E. Zanoria, and S. Danyluk, Surface free energy model of silicon anisotropic etching, J. Electrochem. Soc. **140,** 1080 (1993).

[42] A. F. Holleman, E. Wiberg, and N. Wiberg, *Lehrbuch der Anorganischen Chemie* (Walter de Gruyter, Berlin, 1995), 101 ed., in German.

[43] Roberto Guerra, Elena Degoli, and Stefano Ossicini, Size, oxidation, and strain in small Si/SiO_2 nanocrystals, Phys. Rev. B **80,** 155332 (2009).

[44] There are 2, 3, 4, and 4.5 MLs of SiO_2 plus Si_3N_4 for the $2 \times Si_{10}$-, $2 \times Si_{35}$-, $2 \times Si_{84}$-, and $2 \times Si_{165}$-approximants separating the NCs. Increasing the inter-NC layer thickness of the combined dielectrics or the thickness of the dielectric at the outer NC facets is not possible at present due to intractability of the DFT computations for > 1500 heavy atoms with the level of theory that we use.

[45] A. Zimina, S. Eisebitt, W. Eberhardt, J. Heitmann, and M. Zacharias, Electronic structure and chemical environment of silicon nanoclusters embedded in a silicon dioxide matrix, Appl. Phys. Lett. **88,** 163103 (2006).

[46] H. Gnaser, S. Gutsch, M. Wahl, R. Schiller, M. Kopnarski, D. Hiller, and M. Zacharias, Phosphorus doping of Si nanocrystals embedded in silicon oxynitride determined by atom probe tomography, J. Appl. Phys. **115,** 034304 (2014).

[47] V. V. Afanas'ev, M. Houssa, A. Stesmans, and M. M. Heyns, Electron energy barriers between (100)Si and ultra-thin stacks of SiO_2, Al_2O_3, and ZrO_2 insulators, Appl. Phys. Lett. **78,** 3073 (2001).

[48] The NIST Reference on Constants, Units and Uncertainties—Fundamental Physical Constants (2014 edition) (2014), https://physics.nist.gov/cgi-bin/cuu/Value?asil (accessed October 9, 2019).

[49] W. Mönch, *Semiconductor Surfaces and Interfaces*, Springer Series in Surface Sciences Vol. 26 (Springer, Berlin, 2001), 3rd ed.

[50] D. R. T. Zahn, N. Esser, C. Müller, W. Richter, C. Stephens, R. Whittle, I. T. McGovern, S. Kulkarni, and W. Braun, Influence of Sb and Bi epitaxial monolayers on the metal/GaAs(110) interface formation, Appl. Surf. Sci. **56-58,** 228 (1992).

[51] T. U. Kampen, R. F. Schmitsdorf, and W. Mönch, Sil-ver Schottky contacts on Si(111): H-(11) surfaces pre-pared by wet-chemical etching, Appl. Phys. A **60,** 391 (1995).

[52] T He, D. A. Corley, M. Lu, N. H. Di Spigna, J. He, D. P. Nackashi, P. D. Franzon, and J. M. Tour, Control-lable molecular modulation of conductivity in silicon-based devices, J. Am. Chem. Soc. **131,** 10023 (2009).

[53] I. H. Campbell, S. Rubin, T. A. Zawodzinski, J. D. Kress, R. L. Martin, D. L. Smith, N. N. Barashkov, and J. P. Ferraris, Controlling Schottky energy barriers in organic electronic devices using self-assembled monolayers, Phys. Rev. B **54,** R14321 (1996).

[54] B. de Boer, A. Hadipour, M. M. Mandoc, T. van Wouden-bergh, and P. W. M. Blom, Tuning of metal work func-tions with self-assembled monolayers, Adv. Mater. **17,** 621 (2005).

[55] X. Crispin, V. Geskin, A. Crispin, J. Cornil, R. Lazzaroni, W. R. Salaneck, and Jean-Luc Brédas, Characterization of the interface dipole at organic/metal interfaces, JACS **124,** 8133 (2002).

[56] R. Otero, A. L. Vázquez de Parga, and J. M. Gallego, Elec-tronic, structural and chemical effects of charge-transfer at organic/inorganic interfaces, Surf. Sci. Rep. **72,** 105 (2017).

[57] Unlike in materials with a reasonably wide band gap, such as Si, electrons in metals can be shifted with a relatively small energy expense of approximately $\pm k_B T$ around the Fermi level.

[58] P. S. Bagus, V. Staemmler, and Christof Wöll, Exchange-like Effects for Closed-Shell Adsorbates: Interface Dipole and Work Function, Phys. Rev. Lett. **89,** 096104 (2002).

[59] P. S. Bagus, Klaus Hermann, and C. Wöll, The interaction of C_6H_6 and C_6H_12 with noble metal surfaces: Electronic level alignment and the origin of the interface dipole, J. Chem. Phys. **123,** 184109 (2005).

[60] N. Koch, A. Kahn, J. Ghijsen, J.-J. Pireaux, J. Schwartz, R. L. Johnson, and A. Elschner, Conjugated organic

molecules on metal versus polymer electrodes: Demonstration of a key energy level alignment mechanism, Appl. Phys. Lett. **82,** 70 (2003).

[61] K. Awazu and H. Kawazoe, Strained Si—O—Si bonds in amorphous SiO$_2$ materials: A family member of active centers in radio, photo, and chemical responses, J. Appl. Phys. **94,** 6243 (2003).

[62] Z. Yin and F. W. Smith, Free-energy model for bonding in amorphous covalent alloys, Phys. Rev. B **43,** 4507 (1991).

[63] R. Walsh, Bond dissociation energy values in silicon-containing compounds and some of their implications, Acc. Chem. Res. **14,** 246 (1981).

[64] E. Zeidler, W. Hackbusch, and H. R. Schwarz, *Oxford User's Guide to Mathematics* (Oxford University Press Inc., New York, 2004) translated from German by Bruce Hunt.

[65] F. Ehrhardt, G. Ferblantier, D. Muller, C. Ulhaq-Bouillet, H. Rinnert, and A. Slaoui, Control of silicon nanoparticle size embedded in silicon oxynitride dielectric matrix, J. Appl. Phys. **113,** 033528 (2013).

[66] A. Savitzky and M. J. E. Golay, Smoothing and differentiation of data by simplified least squares procedures, Anal. Chem. **36,** 1627 (1964).

[67] K. W. Böer, *Survey of Semiconductor Physics* (Van Nostrand Reinhold, New York, 1990), Vol. 1.

[68] F. Offi, S. Iacobucci, P. Vilmercati, A. Rizzo, A. Goldoni, M. Sacchi, and G. Panaccione, Attenuation lengths of low-energy electrons in solids: The case of CoO, Phys. Rev. B **77,** 201101(R) (2008).

[69] S. Iacobucci, F. Offi, P. Torelli, and L. Petaccia, Effective attenuation lengths of low energy electrons in MgO thin films, J. Electron Spectr. Related Phenomena **233,** 1 (2019).

[70] M. P. Seah and W. A. Dench, Quantitative electron spectroscopy of surfaces: A standard data base for electron inelastic mean free paths in solids, Surf. Interface Anal. **1,** 2 (1979).

[71] J. W. Keister, J. E. Rowe, J. J. Kolodziej, H. Niimi, T. E. Madey, and G. Lucovsky, Band offsets for ultrathin SiO$_2$ and Si$_3$N$_4$ films on Si(111) and Si(100) from photoemission spectroscopy, J. Vac. Sci. Tech. B **17,** 1831 (1999).

Correction: The inline equation appearing in the sixth paragraph of Sec. V A contained minor errors and has been fixed.